# Recovering paleoearthquake slip record in a highly dynamic alluvial and tectonic region (Hope Fault, New Zealand) from airborne lidar

I. Manighetti, C. Perrin, S Dominguez, S Garambois, Y. Gaudemer, J. Malavieille, L. Matteo, E. Delor, C. Vitard, S Beauprêtre

HAL Id: insu-01469219

https://insu.hal.science/insu-01469219

Submitted on 16 Feb 2017

**Key Points:**
- New airborne lidar data reveal >200 lateral offsets on eastern Hope Fault
- Statistical analysis of offsets reveals a rich record of paleoearthquake slips
- Large paleoearthquakes on eastern Hope Fault recurred by multiples of about 4 m

**Correspondence to:**
I. Manighetti,
manighetti@geoazur.unice.fr

# Recovering paleoearthquake slip record in a highly dynamic alluvial and tectonic region (Hope Fault, New Zealand) from airborne lidar

I. Manighetti[1], C. Perrin[1], S. Dominguez[2], S. Garambois[3], Y. Gaudemer[4], J. Malavieille[2], L. Matteo[1], E. Delor[1,3], C. Vitard[1], and S. Beauprêtre[3]

[1]GEOAZUR, Université de Nice Sophia Antipolis, CNRS, OCA, Nice, France, [2]Géosciences Montpellier, CNRS, Montpellier, France, [3]ISTerre, Université Grenoble Alpes, CNRS, Grenoble, France, [4]Institut de Physique du Globe de Paris, Sorbonne Paris Cité, Université Paris Diderot, CNRS, Paris, France

**Abstract** Knowing the slip amplitudes that large earthquakes produced in prehistorical times is one key to anticipate the magnitude of large forthcoming events. It is long known that the morphology is preserving remnants of paleoearthquake slips in the form of fault-offset landforms. However, the measured offsets that can be attributed to the most recent paleoearthquakes are generally few along a fault, so that they rarely allow recovering the slip distributions and largest slips of these earthquakes. We acquired ~1 m resolution airborne lidar data on a 30 km stretch of a fast-slipping strike-slip fault (eastern Hope Fault, New Zealand) located in a region of high alluvial dynamics where landforms are rapidly evolving. Data analysis reveals >200 offset landforms; only 30% allow a good to moderate quality offset measurement. From these good to moderate quality measures, we recover the slip-length distributions and largest slips of the four most recent large paleoearthquakes and find evidence of 4–6 prior events. The record suggests that large earthquake slip recurred in multiples of about 4 m along the 30 km stretch. Although they have larger uncertainties, the more numerous lower-quality offsets that we also measured reveal a similar earthquake slip record. This shows that, although offset landforms are partly degraded in dynamically active landscapes, they store valuable information on paleoearthquake slips. This information might be recovered provided that the morphology is analyzed at high resolution and "continuously" over a significant fault length. Remote lidar data are powerful to perform such analyses.

## 1. Introduction

Seismic hazard assessment requires properly anticipating the principal characteristics of the forthcoming large earthquakes, especially their expected magnitude or maximum coseismic slip and their recurrence time. One approach to estimate the awaited slip quantities of a forthcoming seismic event on a fault is to analyze the large earthquakes that broke the fault in the prehistorical time (i.e., paleoearthquakes) and to search whether the displacements they produced at the ground surface are still preserved and measurable in the morphology [e.g., *Peltzer et al.*, 1988; *Yeats and Prentice*, 1996; *McCalpin*, 1996, 2009; *Tapponnier et al.*, 2001; *Gold and Cowgill*, 2011; *Li et al.*, 2012; *Zielke et al.*, 2012; *Scharer et al.*, 2014]. This is not an easy task however, for several reasons [e.g., *McCalpin*, 2009; *Scharer et al.*, 2014]. Commonly, the landforms that best act as strain markers and strain recorders, especially along strike-slip faults, are fluvial and alluvial landforms [e.g., *Wallace*, 1968; *Sieh*, 1978; *Gaudemer et al.*, 1989; *McGill and Sieh*, 1991; *McCalpin*, 1996, 2009; *Arrowsmith and Zielke*, 2009; *Zielke et al.*, 2010, 2012]. A first prerequisite is thus that these specific landforms exist along the fault under study. Second, to discriminate the successive large earthquake slips that occurred on a fault, one needs to be sure that the geomorphic markers that recorded these slips formed more frequently than the surface-rupturing paleoearthquakes [e.g., *McCalpin*, 1996, 2009; *Zielke et al.*, 2012; *Salisbury et al.*, 2012]. Third, the original pattern of the geomorphic markers might be modified subsequent to their fault offset as the alluvial (i.e., erosion, incision, sedimentation, modification of the drainage network) and the tectonic (i.e., repeated fault slips, diffuse deformation around the fault) processes are going on [e.g., *McCalpin*, 1996, 2009; *Ouchi*, 2005; *Klinger et al.*, 2011; *Burbank and Anderson*, 2011; *Zielke et al.*, 2012], thereby providing an altered record of the past fault slips. Fourth, because earthquake slip markedly varies along a rupture length [e.g., *Manighetti et al.*, 2005; *Biasi and Weldon*, 2006; *Hecker et al.*, 2013; *Nissen et al.*, 2014], paleoearthquake slips that are measured locally might be different

from the actual maximum or mean coseismic slip amplitudes that must be known to properly estimate the earthquake magnitude [e.g., *Hanks and Kanamori*, 1979]. Finally, as large earthquakes repeat on a fault, the successive coseismic slips add up to form cumulative displacements [e.g., *Wallace*, 1968; *Peltzer et al.*, 1988; *Gaudemer et al.*, 1989; *McCalpin*, 1996, 2009; *Ouchi*, 2005]. These cumulative offsets are the quantities that might be measured in the morphology. However, the amplitude of a cumulative offset is not enough information to infer the number of earthquake slips that added to form it [e.g., *Zielke et al.*, 2012].

Since the landmark paper of *Wallace* [1968], a large number of morphological studies have been conducted to measure fault cumulative offsets and derive information on paleoearthquake slips and fault slip rates [e.g., *Sieh*, 1978, 1984; *Armijo et al.*, 1989; *Gaudemer et al.*, 1989, 1995; *McGill and Sieh*, 1991; *Knuepfer*, 1992; *Van der Woerd et al.*, 1998; *Lasserre et al.*, 1999; *Tapponnier et al.*, 2001; *Hubert-Ferrari et al.*, 2002; *Langridge and Berryman*, 2005; *Gold et al.*, 2011; *Li et al.*, 2012; *Zielke et al.*, 2010, 2012]. Most of these studies were based on field observations. They generally provided accurate offset measurements, demonstrating that the morphology retains a relevant memory of the prehistorical earthquakes [e.g., *Peltzer et al.*, 1988; *McGill and Sieh*, 1991; *Gaudemer et al.*, 1995; *Lasserre et al.*, 1999]. However, because field observations are hampered by vegetation cover and access conditions, field offset measurements are relatively few along most faults worldwide (example: ~20 cumulative offsets measured on the ~400 km long Alpine Fault, New Zealand [e.g., *Berryman et al.*, 2012; *De Pascale et al.*, 2014]). Except when the fault ruptured in historical time, small cumulative offsets (i.e., <10–20 m) produced by the most recent large earthquakes are especially few in the field measurements [e.g., *Zielke et al.*, 2012], because small offsets are often rapidly degraded whereas their identification and measure request high-resolution observations (example: 9 offsets < 10 m measured on the ~400 km long Alpine Fault, New Zealand [e.g., *De Pascale et al.*, 2014; see discussion in *Scharer et al.* [2014]).

In the last decade, the development of the airborne lidar technology and other high-resolution satellite imagery techniques has launched a new form of "remote-sensing paleoseismology" [e.g., *Zielke et al.*, 2010, 2012; *Klinger et al.*, 2011; *Meigs*, 2013; *Scharer et al.*, 2014]. The lidar laser pulse has the ability to hit the ground under vegetation, and hence, lidar data provide an unprecedented topographic measure of "bare Earth," at a very high resolution (ground pixel resolution in the range of 0.5–5 m depending on vegetation density [e.g., *Lin et al.*, 2013; *Langridge et al.*, 2014]) and over long fault sections (swaths of several tens of kilometers long and 1–2 km wide [e.g., *Haugerud et al.*, 2003; *Sherrod et al.*, 2004; *Bevis et al.*, 2005; *Kondo et al.*, 2008; *Barth et al.*, 2012; *Zielke et al.*, 2012; *Lin et al.*, 2013; *Langridge et al.*, 2014]). Airborne lidar data thus allow observations and measurements in places not accessible before, and as such, they provide a new powerful tool to remotely analyze the morphology and its earthquake slip record. An increasing number of lidar-based (or high-resolution image-based) studies have thus been conducted in the last few years, mostly to analyze the coseismic strain field of recent earthquakes [e.g., *Oskin et al.*, 2012; *Nissen et al.*, 2014] or to examine the morphological record of historical and prehistorical earthquakes [e.g., *Zielke et al.*, 2010, 2012; *Klinger et al.*, 2011; *Haddad et al.*, 2012]. The latter studies have provided 10–20 times more measurements of cumulative offsets than ever before, thereby demonstrating that remote lidar and high-resolution data can be used to recover a rich paleoseismological information. Not only the 2–4 most recent large earthquakes were identified and discriminated in the remote measurements but also their slip-length function could be reconstructed in the lidar (or image) stretch [e.g., *Zielke et al.*, 2010; *Klinger et al.*, 2011; *Zielke et al.*, 2012].

The remote data-based paleoseismological studies listed above have targeted major strike-slip faults in rather arid climates (remote sections of San Andreas Fault in California [e.g., *Frankel et al.*, 2007; *Arrowsmith and Zielke*, 2009; *Zielke et al.*, 2010, 2012] and Fuyun Fault in China [e.g., *Klinger et al.*, 2011]). In such contexts, erosion is generally moderate [e.g., *Klinger et al.*, 2011], which favors the good preservation of fault-offset landforms. Here we question whether, in a much less favorable context of landform preservation, airborne lidar data may still provide useful information on paleoearthquake slips. We target a major (~230 km long), fast-slipping (~23 mm/yr), seismogenic strike-slip fault (Hope Fault, New Zealand) located in an environment where rainfalls, sediment supply, and hence alluvial dynamics have been high over the Holocene up to present time [e.g., *Bull*, 1991]. In such a "humid" climate (as defined by *Bull* [1991]), it is expected that multiple alluvial landforms have been created over time, thereby forming numerous potential fault slip recorders. But it is also expected that some of the offset landforms have rapidly degraded over time as the alluvial and tectonic processes were going on at fast rates. Therefore, in
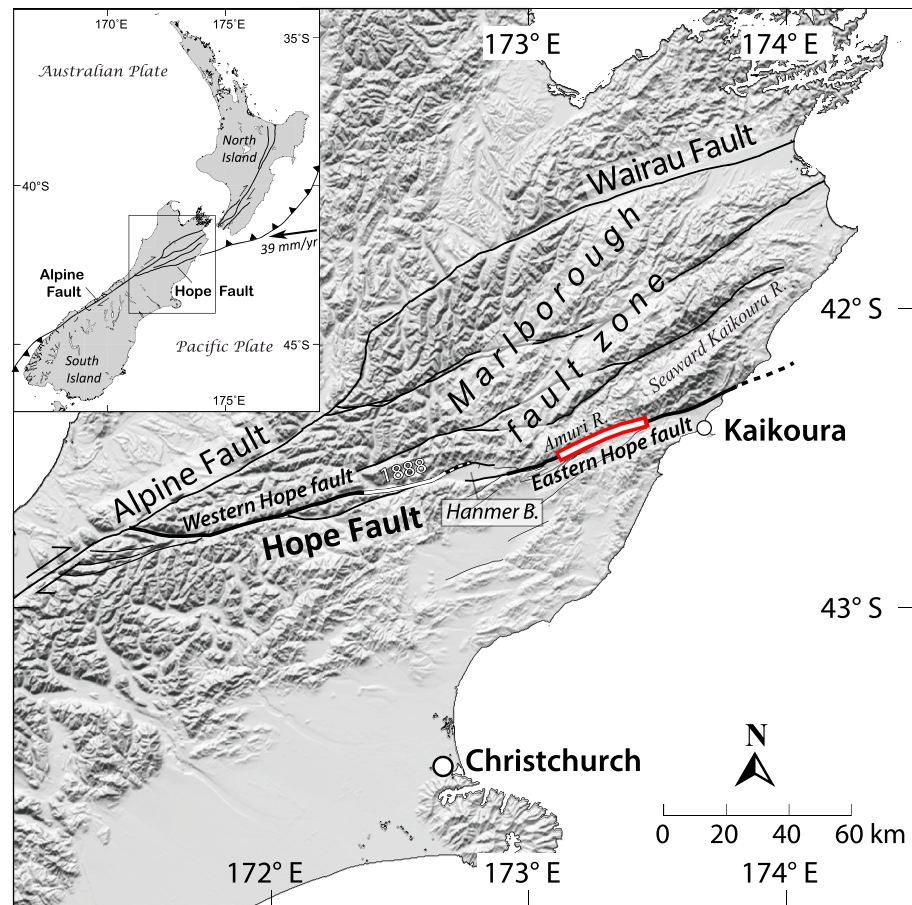
**Figure 1.** Tectonic setting of Southern Island of New Zealand and location of the Hope Fault. The zone covered with the lidar data is shown as a red box. The 1888 rupture zone is indicated with a white line.

such a context of high alluvial and tectonic dynamics, it is not clear whether the geomorphic records can be used to recover the earthquake slip history. Field measurements available on the Hope Fault prove that some paleoseismological information is preserved in the morphology [e.g., *Cowan and McGlone*, 1991; *Yang*, 1991; *Knuepfer*, 1992; *Langridge et al.*, 2003, 2013; *Langridge and Berryman*, 2005], but these measurements are too few (i.e., 10 offsets < 60 m on eastern Hope Fault that we analyze; see section 2) to discriminate confidently the paleoearthquakes and to determine the slips they produced all along the fault.

We have acquired airborne lidar data on the eastern Hope Fault to analyze the morphology at a high resolution over a 30 km long stretch of the fault. The lidar data reveal fault offsets that were not accessible to observation before. We show that, although the geomorphic landforms offset by the eastern Hope Fault show complex and partly degraded traces, when these offset landforms are examined at high resolution, measured densely and analyzed collectively along a significant length of the fault, they prove to retain a rich information on the few most recent prehistorical large earthquakes. These paleoearthquakes can be discriminated while their slip-length function can be recovered in the lidar stretch. Ultimately, we use the preserved record to discuss the seismogenic behavior of the eastern Hope Fault.

## 2. Tectonic and Alluvial Setting of the Eastern Hope Fault

The ~230 km long, N75° striking Hope Fault is one of the longest right-lateral faults of the Marlborough relay zone between the dextral Alpine Fault in the southwest and the North Island dextral faults in the northeast (Figure 1) [e.g., *Lensen*, 1968; *Freund*, 1971; *Van Dissen*, 1989; *Cowan*, 1990; *Berryman et al.*, 1992; *Little and Jones*, 1998; *Barnes and Audru*, 1999a, 1999b]. The Hope Fault is fast slipping, with lateral and reverse Quaternary slip rates of $23 \pm 4$ and ~2 mm/yr, respectively [e.g., *Van Dissen*, 1989; *Cowan*, 1989, 1991;

*Cowan and McGlone*, 1991; *McMorran*, 1991; *Berryman et al.*, 1992; *Knuepfer*, 1992; *Langridge et al.*, 2003; *Langridge and Berryman*, 2005]. The fault is divided in two, ~100 km long, western and eastern major segments (Geological and Nuclear Sciences active fault database: http://data.gns.cri.nz/af/) separated by the central, 6–7 km wide Hanmer pull-apart (Figure 1) [*Cowan*, 1990; *Wood et al.*, 1994]. In the following, we refer to the western and the eastern segments as the western and the eastern Hope Fault, respectively [*Langridge et al.*, 2003]. The eastern Hope Fault might continue over 20–25 km offshore [*Barnes and Audru*, 1999a, 1999b], and thus, its total length might be up to ~120 km. Here we analyze an ~30 km long stretch of the eastern Hope Fault, whose western edge starts ~15 km east of the junction between the fault and the Hanmer pull-apart (Figure 1).

The 1888 "North Canterbury" earthquake ($M_w$ 7.1–7.3) is the only large historical earthquake known on the Hope Fault. It broke the eastern end of the western Hope Fault over a minimum length of 30 km (Figure 1; rupture length ≥100 km has been suggested by *Knuepfer* [1984]) and produced lateral displacements of at least 2.6 m [*McKay*, 1890; *Cowan*, 1991; *Cowan et al.*, 1996; *Stirling et al.*, 2012]. In an attempt to recover longer past earthquake histories on the Hope Fault, numerous morphotectonic and trench-paleoseismological studies have been conducted (synthesis in *Langridge et al.* [2013]). Table S1 in the supporting information synthesizes the lateral offset field measurements that are presently available, to the best of our knowledge, on the eastern (Table S1a in the supporting information) and on the western Hope Fault (Table S1b in the supporting information). While these measurements are numerous on the western Hope Fault, they are few on the eastern Hope Fault (~20). Small lateral offsets supposed to record the most recent earthquakes are particularly few, with only 10 measured offsets lower than ~60 m. From these few measurements, it has been inferred that the most recent large earthquake on the eastern Hope Fault produced a lateral slip at surface in the 3 to 6 m range [*Knuepfer*, 1992; *Pope*, 1994; *Langridge et al.*, 2003]. Meanwhile, the synthesis of the numerous trench results suggests that 2–3 large paleoearthquakes broke separately the western and the eastern Hope Fault, at two similar periods, 700–400 and 360–120 year ago [*Langridge et al.*, 2013, and references therein].

Bounding the high (>1600 m) seaward Kaikoura and Amuri Ranges, the eastern Hope Fault separates steep, large drainage basins from low-relief piedmont terrain [e.g., *Bull*, 1991]. The drainage basins are underlain by folded and faulted massive greywacke of the Mesozoic Pahau terrane [*Rattenbury et al.*, 2006]. Alternating aggradation and degradation episodes have occurred repeatedly during the late Quaternary downstream from the eastern Hope Fault [e.g., *Bull*, 1991], inducing the development of a dense alluvial network and the accumulation of multiple generations of Quaternary alluvial deposits, especially terraces [*Knuepfer*, 1988; *Bull*, 1991; *Tonkin and Almond*, 1998]. The Holocene was a period of heavy rainfall episodes, due to the warmer climate that followed the prior glacial stage [*McGlone*, 1988; *Bull*, 1991], and was therefore "characterized by excess stream power that promoted stream-channel downcutting" [*Bull*, 1991]. Tropical storms were also likely during the Holocene [*Bull*, 1991]. Therefore, the alluvial dynamics were high in the eastern Hope Fault region over the Holocene, and it is thus likely that a large number of alluvial landforms formed repeatedly during that period.

## 3. Mapping of the Fault and of the Offset Markers

### 3.1. Lidar Data

The lidar data cover an ~1 km wide section of the eastern Hope Fault (red quadrant in Figure 1 and Figure 2). The data were acquired and processed by New Zealand Aerial Mapping Limited. They allow the surface topography to be described at all places including those covered with vegetation, with a mean point density of 1.2 pt m$^{-2}$ and a vertical precision of 5–10 cm. However, the ground return point density varies depending on the vegetation cover [e.g., *Lin et al.*, 2013; *Langridge et al.*, 2014]. The zone under study includes a few small spots of fairly dense vegetation (representing ~10% of the lidar stretch), where the average number of ground returns is 0.5–0.6 pt/m$^2$. However, none of the offset markers retained in the present analysis locate in those zones. About 15–20% of the lidar stretch is covered with relatively sparse and low vegetation, where the average number of ground returns is 1–1.5 pt/m$^2$. Over the rest and majority of the area, the ground shows no or very short vegetation and has an average number of ground returns in the range of 1.8–3 pt/m$^2$. Therefore, most markers and lateral offsets that we describe in the following are resolved at a maximum 1 m horizontal uncertainty and generally with a greater precision. To
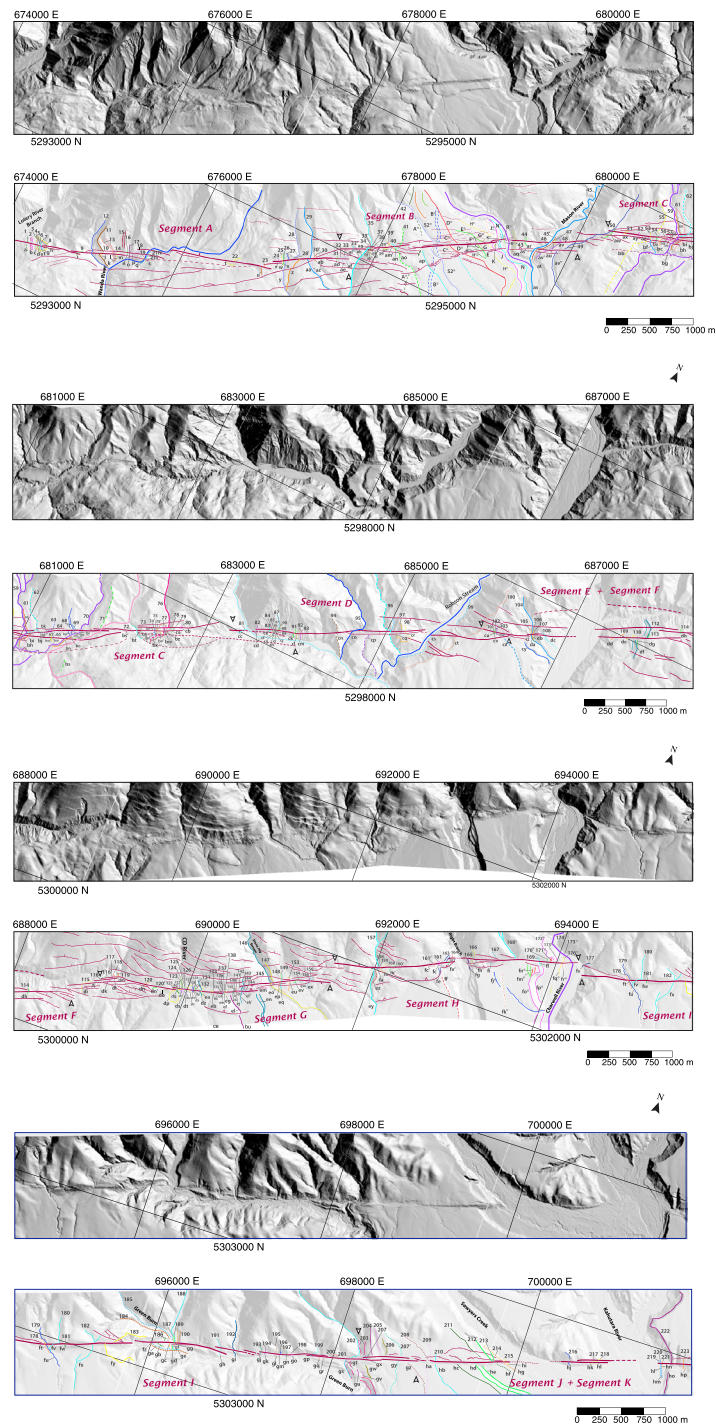
**Figure 2.** Views of the lidar data and morphotectonic mapping of the faults and of the offset alluvial and morphological markers. For clarity, the ~30 km fault section has been divided into four images that slightly overlap and that are presented from west to east. The morphology is illuminated from the north in all images. The ends of the A to K fault segments are indicated with white arrows. All the markers described in the present study are mapped, in different colors, with their names indicated and reported in Table S2 in the supporting information along with the offset values and details on the markers. In dotted are the quality 4 markers whose lateral offsets could not be measured confidently. Note that the mapping was done primarily to locate the multiple markers and hence is not precise in the greatest details (Figures 3 and 4 and Figure S1 in the supporting information provide more detailed images of many of the markers). The offset measurements were conducted on the actual morphological traces, not on the mapped traces (see examples in Figures 3 and 4 and Figure S1 in the supporting information). The markers that were previously described in the literature are indicated with a star (references in Table S2 in the supporting information).

account for the variability of the lidar data density at the scale of the entire 30 km long stretch, we represent the lidar-derived digital elevation model (DEM) as a $1 \times 1$ m grid (Figure 2). However, to account for the greater precision of the lidar data for most offset markers, we have produced a 0.5 m elevation contour DEM which we use to perform the offset measurements.

We analyzed the lidar data using the ERDAS ER Mapper software (http://geospatial.intergraph.com) that allows visualizing the topographic data at any scale and in different ways (see below), while multiple georeferenced data can be superimposed and analyzed together (such as geological maps and orthophotos acquired with the lidar data). To identify and map the fault traces and the offset markers, we examined four complementary representations of the topographic lidar data: a sunlit, hill-shade representation with variable Sun shading, which allows a clear identification of the fault traces and of the offset features, even small; a slope representation, helpful to locate the fault scarps and to identify markers such as streambeds and flanks, terrace risers, and scarps of any type; a dip (or "azimuth") representation, which helps the recognition of similar features, even small, either side of the fault; and a 0.5 m contour line representation (complemented with a 0.25 m plot in a few cases), which provides a precise, quantitative guide to measure the lateral offsets.

### 3.2. Fault Trace

We first analyzed the lidar data to map the fault trace in detail. The eastern Hope Fault has already been mapped in several prior works [e.g., *Clayton*, 1966; *Freund*, 1971; *Hardy and Wellman*, 1984; *Van Dissen*, 1989; *Yang*, 1991; *Barnes and Audru*, 1999a, 1999b; *Eusden et al.*, 2000, 2005; *Khajavi et al.*, 2014], but the lidar data provide a more precise vision of its trace. Consistently with its right-lateral motion, fast slip rate and current activity, and as recognized in prior studies, the fault shows a pronounced, narrow, linear overall trace that can be followed almost continuously across the lidar stretch. In more details, the fault trace divides, in the analyzed section, into 11 left-stepping en echelon short segments (labeled A to K in Figure 2) of roughly similar lengths (1–3 km), generally separated by 100–200 wide step-overs of push-up or pull-apart types (Figure 2). Some of the A–K segments are themselves divided into a few shorter left-stepping segments. Locally, the surface expression of the fault forms a small (<1–20 m high), generally south facing scarp. The main fault trace is associated with adjacent secondary, short, dip-slip faults, whose arrangement and slip mode are consistent with the right-lateral motion on the principal fault strand (Figure 2). The fault cuts across the dense drainage network that dissects the Kaikoura and Amuri Ranges, and laterally offsets most of the numerous river-, stream-, and channel beds, floodplains, alluvial terraces, and risers, and alluvial fans that extend at the foothills of the range. In the following, we call "marker" any such alluvial and/or morphological features offset by the fault.

### 3.3. General Description of the Offset Markers

We recognized and mapped 214 markers laterally offset along the fault (Figure 2 and Table S2 in the supporting information, where markers are described and offset measurements provided), but we measured a lateral offset for only 134 of them; for the remaining 80 markers, the lateral offset exists but is too complex to be measured confidently in the present lidar data (for reasons explained in Table S2 in the supporting information). About 65% of the identified offset markers are stream channels of various sizes (active or abandoned, expressed by their beds and/or banks) and terrace risers, but a few others are alluvial fans, landslide/debris deposits, gravitational failure scarps, undefined erosional scarps, and small topographic reliefs along the fault, as described in previous studies [e.g., *Khajavi et al.*, 2014].

In an idealized case of a strike-slip fault in a well-preserved environment, the existence of a lateral offset is commonly attested by specific, long-recognized, patterns [e.g., *Wallace*, 1968, 1990; *Peltzer et al.*, 1988; *Gaudemer et al.*, 1995; *McCalpin*, 1996, 2009; *Yeats et al.*, 1997; *Van der Woerd et al.*, 2002, 2006; *Ouchi*, 2005; *Burbank and Anderson*, 2011; *Klinger et al.*, 2011; *Zielke et al.*, 2010, 2012; *Zielke and Arrowsmith*, 2012]. A prerequisite is that the offset marker has a straight, narrow trace approximately perpendicular to the fault, which has also a narrow trace. Then, several patterns can be observed: (i) the marker has its trace clearly recognizable on either side of the fault, yet its trace is interrupted and laterally offset across the fault without any significant change in its shape and trend (sharp bayonet kink at the fault [e.g., *Bell et al.*, 1997]; see examples in Figures 3a and 3b and Figure 4 and additional examples in Figure S1 in the supporting information; these figures are described further below); (ii) the marker has its trace clearly
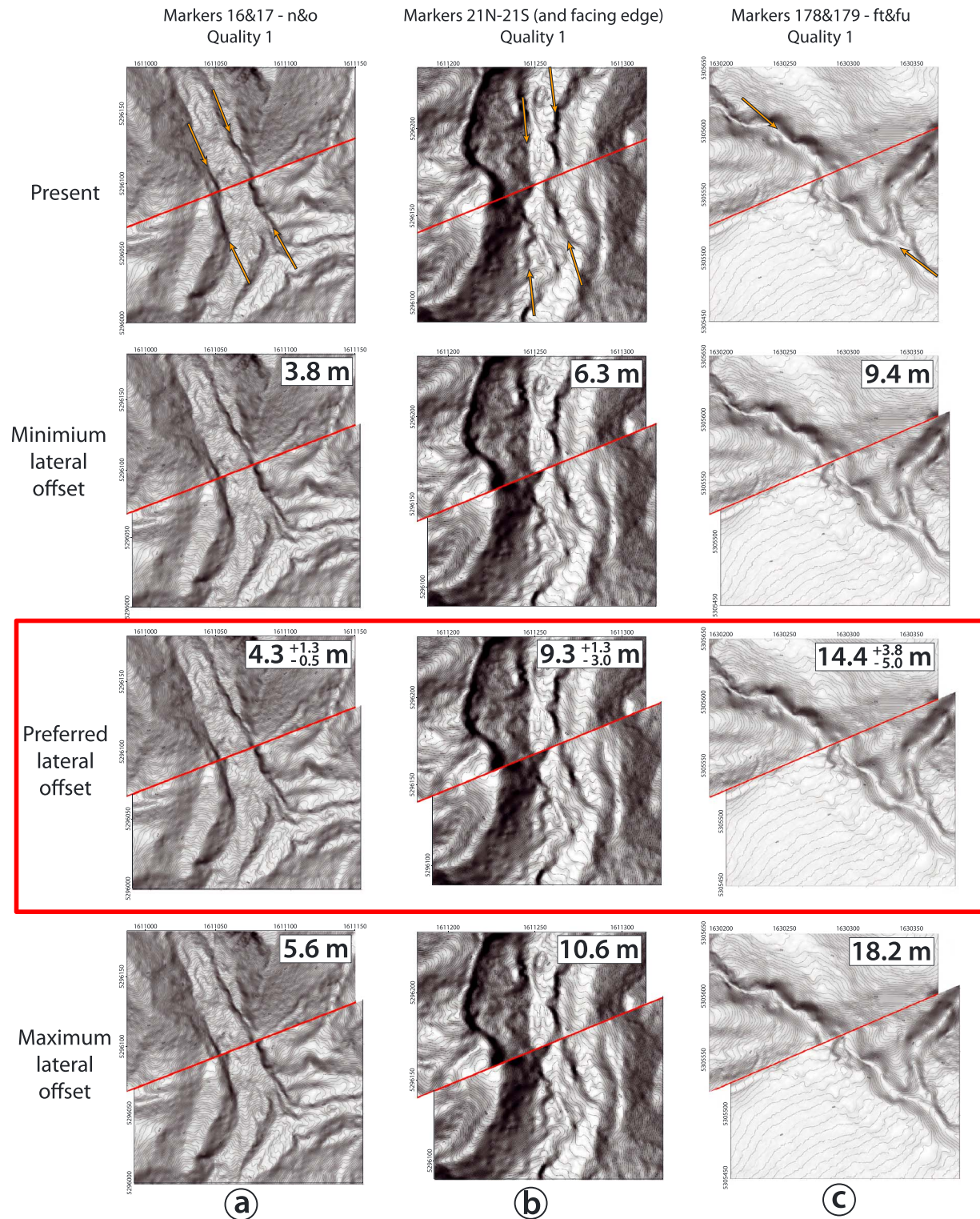
**Figure 3.** Examples of back slip reconstructions of offset markers and measurement of their lateral offset. Three examples are shown, with their name, lateral offset, and quality indicated (location in Figure 2 and description in Table S2 in the supporting information). The examples illustrate three of the four offset values best preserved in the morphology, i.e., around 4, 9, and 14 m (see Figure 5). The figures are combined hillshade and contour plots (0.5 m). The fault trace is in red. The orange arrows in top plots indicate the (a and b) marker edges or (c) the marker overall trend. Position of arrows is only indicative, the actual trace of the markers being better seen in the reconstructed plots. Preferred, optimal offset is shown in red quadrant, whereas minimum and maximum offset values that yield a plausible reconstruction of the original marker shape are shown on either side. When the marker is a channel, the minimum and maximum offsets are estimated by restoring each of the two channel flanks.
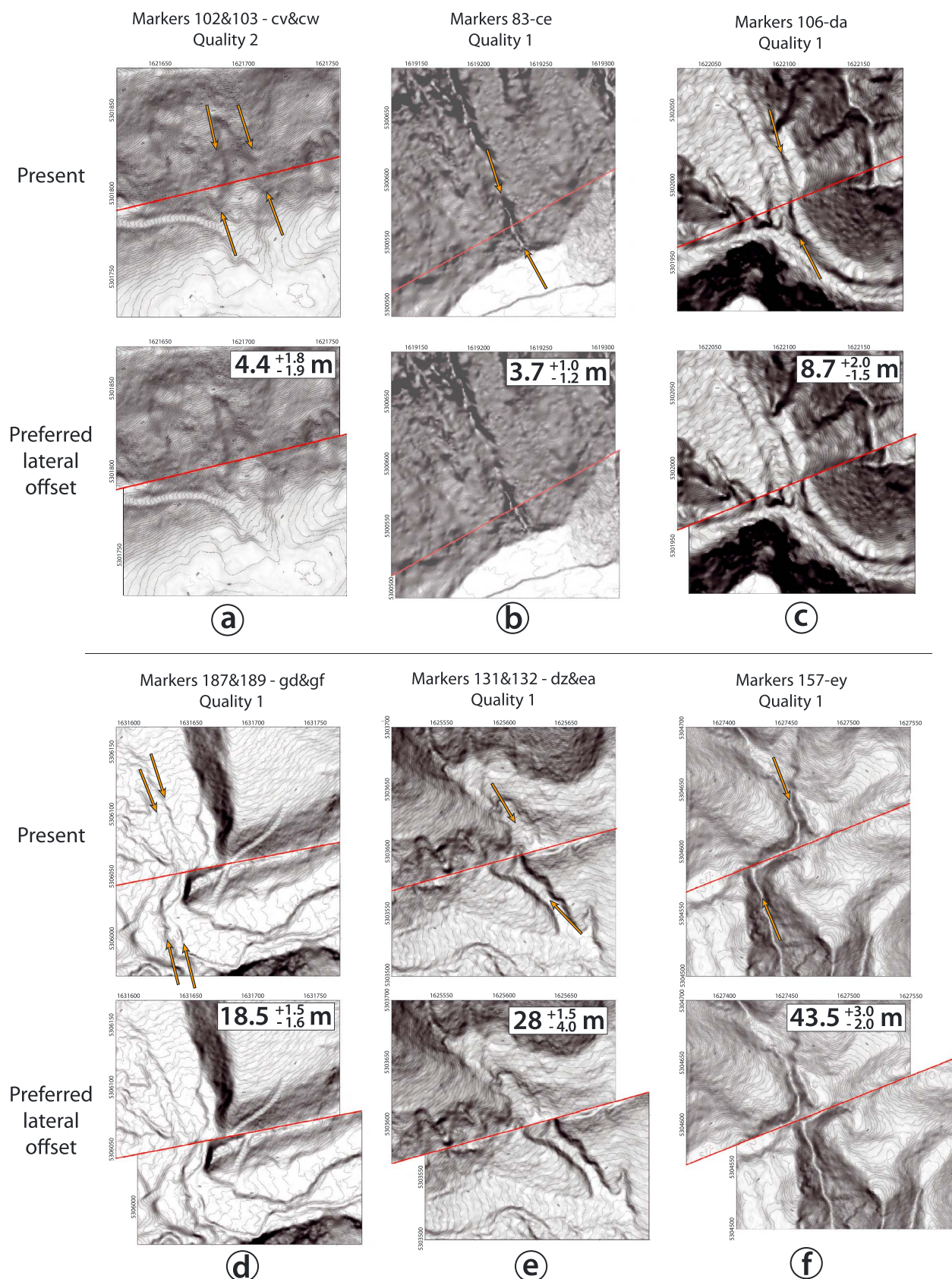
**Figure 4**

recognizable and continuous on either side of the fault, yet its trace is laterally deflected and warped across the fault so that it looks like a *S* close to the fault (smooth bayonet [e.g., *Gaudemer et al.*, 1995; *Lacassin et al.*, 1998]; see examples in Figures 3c and 4b, respectively, and additional examples in Figure S1 in the supporting information). Note that the *S* trace nearby the fault (the "offset reach" as defined in *Ouchi* [2005]) can be laterally displaced subsequent to its formation (see example 35'-ah in Figure S1 in the supporting information); and (iii) a marker section has its trace in one fault side that looks similar in shape to the trace of a *nearby* marker section of same alluvial or morphological nature in the other fault side (see examples in Figures 4a and 4c–4e and additional examples in Figure S1 in the supporting information).

We used these patterns to identify and measure the lateral offsets. However, the offset geometries generally revealed to be more complex than the ideal cases described above (see examples in Figure S1 in the supporting information): many of the markers' traces show small-wavelength sinuosity, or are curved, or oblique to the fault, or have a strike that changes across the fault; the incision varies across the fault, being generally deeper in the northern compartment (because of a small reverse component [e.g., *Eusden et al.*, 2000]), and thus, the 3-D pattern of some offset markers differs either side of the fault; some of the offset channels have been captured by displaced streams; and some of the offset markers seem to have been markedly degraded (weathered traces). We interpret these complexities to result from the combined effects of the ongoing, high-dynamic alluvial and tectonic processes that progressively modify and/or degrade the geomorphic landforms. Therefore, measuring lateral offsets along the eastern Hope Fault is less straightforward than in the ideal cases previously described.

The geological map of the fault area [*Rattenbury et al.*, 2006], along with other available stratigraphic information [*Bull*, 1991; *Knuepfer*, 1992] (see Tables S1 and S2 in the supporting information), shows that the vast majority (~70%) of the markers that we identified (Figure 2) incise or overlay late Quaternary deposits whose maximum ages are approximated to ~12 ka [*Rattenbury et al.*, 2006]. Most identified offset features are thus of Holocene age, as shown in Table S1 in the supporting information. We infer that most markers have experienced humid climatic conditions during their geomorphic and tectonic evolution.

## 4. Measurement of the Fault Lateral Offsets

Although it has a small component of reverse slip [e.g., *Eusden et al.*, 2000], the Hope Fault is dominantly strike slip, and hence, we focused on measuring the lateral cumulative displacements. The lateral to vertical slip ratio being high on the fault (≥~10 [e.g., *Knuepfer*, 1992; *Langridge and Berryman*, 2005; *Langridge et al.*, 2013]), the horizontal offsets provide a fair estimate of the actual fault slips.

Below we describe the way we measured the lateral fault offsets and the two types of uncertainties that affect the measurements. We use the term "correlation" to refer to the recognition of two marker sections that were, or are considered to have been, contiguous originally before the fault motion separated them.

### 4.1. Back Slipping Approach to Measure Lateral Offsets

Cumulative lateral offsets on strike-slip faults have been measured for decades using the so-called "back slipping approach" [e.g., *Sieh*, 1978; *Rockwell et al.*, 1990; *Ritz et al.*, 1995; *Klinger et al.*, 2000, 2005, 2011; *Van der Woerd et al.*, 2002, 2006; *Haibing et al.*, 2005; *Mériaux et al.*, 2005; *Oskin et al.*, 2007; *Zielke et al.*, 2010, 2012; *Rizza et al.*, 2011, 2015]. The fault is approximated as a vertical plane across which most of the lateral slip occurs. These simple assumptions are supported by observations on natural faults. In particular, while secondary faulting is commonly observed off major fault traces [e.g., *Cappa et al.*, 2014], in strike-slip

**Figure 4.** Additional examples of back slip reconstructions and lateral offset measurements. Here for clarity, only the preferred, optimal lateral offset is shown, being compared with the present marker trace. The figures are combined hillshade and contour plots (0.5 or 1 m). The fault trace is in red. The orange arrows in top plots indicate the (a, c, and d) marker edges or the (b, e, and f) marker overall trend. Position of arrows is only indicative, the actual trace of the markers being better seen in the reconstructed plots. Six examples are shown, with their name, lateral offset, and quality indicated (location in Figure 2 and description in Table S2 in the supporting information). The examples illustrate three of the offset values best preserved in the morphology (i.e., around 4, 9, and 18 m) and two larger offset values also preserved, although more partially (i.e., around 28 and 44 m) (see Figure 5).

**Table 1.** Criteria to Discriminate the Four Quality Ratings of the Lateral Offsets[a]

| Quality | Description | % of the Total Offset Population |
|---|---|---|
| 1 | The marker is well preserved, has a simple trace, and still shows clearly its original continuity across the fault. The correlation of the two marker's sections is thus unambiguous. Furthermore, the marker is at a high angle to the fault. Its trace shows clearly in the four data representations, elevation contours, hillshade, slope, and azimuth. The marker is fully resolved in the lidar data (<1 m). | 9 |
| 2 | The marker is well preserved overall, and the correlation of the two marker's sections across the fault is unambiguous. However, the marker has either a subtle trace, or has a trace at a moderate angle to the fault (yet >~50°), or has a trace that might have been slightly eroded. The marker shows clearly in at least two of the data representations, among elevation contours, hillshade, slope, and azimuth. The marker is fully resolved in the data (<1 m). | 20 |
| 3 | The two marker sections are recognized on either sides of the fault, and their correlation is likely, but the two marker sections are now at a significant distance from one another, or they seem to have been partly eroded, or they have a trace with a complex form, or they strike at a moderate angle to the fault (<~50°). The marker shows clearly in one or two of the data representations among elevation contours, hillshade, slope, and azimuth. The marker is either fully resolved in the data (≤1 m) or more poorly resolved with a pixel resolution between 1 and 2 m. | 34 |
| 4 ➜ not included in present analysis | The two marker sections are recognized on either sides of the fault, but their correlation might be debatable, or the marker is poorly resolved in the lidar data, or the offset measurement is redundant with another, nearby, better constrained measurement. | 37 |

[a]The percentage of offsets in each population is indicated.

contexts slip partitioning generally occurs between on-fault lateral and off-fault vertical slip components [e. g., *Armijo et al.*, 2002], as observed for the eastern Hope Fault. Since the landforms are laterally offset by a subvertical strike-slip fault, it is their *x-y* planform geometry that most records the lateral offsets [e.g., *Ouchi*, 2005]. The back slipping approach aims at reconstructing the original planform geometry of the offset markers. It consists of cutting along the fault trace a rasterized representation of the topography and then of moving it parallel to the fault in a sense opposite to the present fault offset until the marker is reconstructed with a realistic original shape. The back slip length then measures the lateral offset. The marker reconstruction is thus made visually. Although this approach contains a part of subjectivity, it is based on the human eye capacity to analyze simultaneously a large area containing multiple and various information and on the expert knowledge of what natural landforms look like. At present, there exists no numerical code able to better reconstruct laterally fault-offset landforms. *Zielke and Arrowsmith* [2012] have developed a 2-D code (LaDiCaoz) to assist the visual back slipping procedure: two short vertical profiles encompassing the two sections of an offset marker either side of a fault are best adjusted numerically (with a goodness of fit criterion) in the *x-z* plan, and this best adjustment is then used to guide the visual back slipping of the marker sections in the *x-y* plan. In Figure S2 in the supporting information, we have measured one fault offset using the back slipping procedure (the measured offset is then $4.3 \pm 1.3$ m) and using an expanded version of the LaDiCaoz code where multiple pairs of vertical profiles extracted at different sites along the marker length are fitted. This expansion of the code allows to better take into account the overall shape of the marker. The best offset results to be $4.7 \pm 1.5$ m. The two methods therefore lead to the same offset value. As only back slipping integrates the planform geometry of the offset markers, we favor the use of this classical approach, as done in most prior works (including *Zielke and Arrowsmith* [2012]).

The offset measurements come along with two types of uncertainties that we now describe.

## 4.2. Quality Rating of the Correlations

Measuring the cumulative lateral offset recorded by a marker requires, first to recognize the two sections of the marker that once were contiguous but are now separated, second to restore properly the original shape of the marker, and third to measure the lateral offset which displaced the original marker, along with the uncertainties on that measurement. The first two steps come along with an epistemic uncertainty that expresses the trust one can have in a correlation [e.g., *McCalpin*, 1996, 2009; *Salisbury et al.*, 2012; *Scharer*

et al., 2014]. For instance, there might be cases where the two marker sections are unambiguously recognized (i.e., they are the two separated pieces of a single feature); yet because their trace is complicated or because erosion has subsequently modified it, there is no way to properly reconstruct the original shape of the offset feature, even though measurements are precisely done (see below). Therefore, the epistemic uncertainty on the correlations can only be expressed qualitatively, and we formulate it as a quality rating as it is commonly done [e.g., *McCalpin*, 2009; *Zielke et al.*, 2012; *Scharer et al.*, 2014, and references therein].

We rate the offset markers into four classes, based on criteria described in Table 1. Offset markers rated as quality 1 look well preserved and are well resolved in the lidar data (resolution ≤1 m), have a simple trace approximately perpendicular to the fault, exhibit clear piercing points onto the fault trace, and still show clearly their original "continuity" across the fault. They are thus unambiguous, whereas their lateral offset can be measured in a straightforward manner in any of the four data representations. These quality 1 "best offsets" represent ~9% of the total offset population and hence are few. All quality 1 offsets ≤60 m are shown in the set of Figures 3 and 4 and Figure S1 in the supporting information (the figures are discussed further below). Offset markers rated as quality 2 look well preserved overall, are well resolved in the lidar data (resolution ≤1 m), and their correlation is unambiguous. However, their trace is either subtle, or oblique to the fault, or might have been slightly eroded, altogether making the restoration of the original marker trace slightly more difficult than for quality 1 offset markers. These quality 2 or "moderate quality offsets" represent ~19% of the total offset population (all quality 2 offsets ≤60 m are shown in the set of Figure 4 and Figure S1 in the supporting information). Offset markers rated as quality 3 are recognized on either side of the fault, and their correlation is likely, but the two marker sections are subtle, or stand at a significant distance from each other, or seem to have been partly eroded, or have a trace with a complex form, or strike at a shallow angle to the fault (<~50°). These markers might be fully resolved in the lidar data (≤1 m) or more poorly resolved with a pixel resolution between 1 and 2 m. These quality 3 or "low-quality offsets" represent ~33% of the total offset population (quality 3 offsets are not shown due to their lower quality). Finally, offset markers rated as quality 4 might be disputable, or are poorly resolved in the lidar data, or have an offset measurement that is redundant with another, nearby, better constrained measurement. These quality 4 or "poor quality" offsets represent ~39% of the total offset population. We exclude them from further analysis. Yet we list them in Table S2 in the supporting information as they might deserve further investigations.

The proportion of good quality offsets is thus very low. The predominance of moderate- to low-quality offsets actually enhances the question we aim to address: does such a complex morphological record preserves valuable information on prehistorical earthquake slips?

### 4.3. Uncertainties on the Offset Measurements

Once a pair of offset marker sections has been recognized and qualified, the lateral offset can be measured with a so-called "random" or "aleatory" uncertainty that describes the range of on-fault slips that yield a plausible restoration of the original marker shape [e.g., *McGill and Sieh*, 1991; *McCalpin*, 1996; *McGill and Rubin*, 1999; *Zielke et al.*, 2012; *Scharer et al.*, 2014]. Provided that the marker has not been significantly eroded, this uncertainty depends mostly on the strike (uncertainties are smaller when markers trend at a high angle to the fault) and overall geometry (curved and sinuous traces make piercing points more ambiguous to identify) of the marker with respect to the fault.

To perform the restorations, we examined and back slipped each marker on the four representations of the lidar data described in section 3. This allowed us to tightly define the optimal lateral offset which best restores the likely original marker shape. Because the contour plots best resolves the actual shape of the displaced small-scale features, we eventually measured the lateral offsets on the elevation contours (except in rare cases of very small markers not sufficiently clear in the contour plots). As is classically done [e.g., *McCalpin*, 2009; *Burbank and Anderson*, 2011], we measured the lateral offsets between the piercing points of the two marker sections, or of their along-strike projection, onto the fault trace. This approach thus ignores the narrow warping zone that might exist along the fault trace [e.g., *Ouchi*, 2005].

To tightly bracket the range of slip that well restores each marker, three of us have performed each measurement a total of 4 to 6 times. The range of uncertainties might be asymmetric with respect to a preferred value, and thus for each offset measurement, we indicate the plus and minus uncertainties

(Table S2 in the supporting information). Examples of minimum, preferred, and maximum offset reconstructions are shown in Figure 3, whereas all other reconstructions of qualities 1 and 2 (for offsets ≤ 60 m) are shown in Figure 4 and Figure S1 in the supporting information. Overall, we have favored large uncertainties (Table S2 in the supporting information). The smallest reported uncertainty coincides with the lidar data horizontal resolution and hence is 1 m in the general case and 0.5 m in a few rare cases. It has to be noted however that, although the lowest "analytical" uncertainty is by definition the pixel size of the lidar DEM, even if one would use more accurate data, it would be likely misleading to suggest uncertainties lower than ~1 m because errors on the lateral offsets mainly reflect the difficulty to restore the complex original morphology of the markers, and this error is generally greater than 1 m.

On average the estimated uncertainties are ~22% of the respective offsets for the entire population. It is noteworthy that uncertainties on offset measurements provided in the literature (on New Zealand faults and other faults worldwide) are generally smaller, commonly less than 10% of the offsets [e.g., *Sieh*, 1978; *Knuepfer*, 1992; *Langridge et al.*, 2003; *Little and Jones*, 1998; *Zielke et al.*, 2010] (see Table S1 in the supporting information for the Hope Fault case). In our data collection, uncertainties ≤ 10% of the slip concern only ~23% of the population. The smallest offsets in the range of 0–20 m (~55% of the offset population) have fairly large uncertainties, on average 30% of the slip, and all but two greater than 10%. These large uncertainties arise from the small offset population including a large number of quality 3 measurements.

## 5. Statistical Analysis of the Lateral Offsets

The 134 offset measurements range between 2.5 and 310 m, with 78% of them ≤ 65 m (Table S2 in the supporting information). With such a dense data collection over such a long fault section (i.e., ~30 km), two issues must be considered, which we describe below.

### 5.1. General Approach

First, as we aim to recover the successive coseismic slips that added over time to build the measured cumulative offsets, we must keep in mind that each of the paleoearthquakes might have produced a variable slip along the section of the fault under analysis [e.g., *Manighetti et al.*, 2005; *Biasi and Weldon*, 2006; *Hecker et al.*, 2013]. Pronounced slip gradients especially occur at fault step-overs [e.g., *Walsh et al.*, 2003; *Davis et al.*, 2005; *Manighetti et al.*, 2009, 2015]. Therefore, to set aside the issue of slip variability along the fault length, we must analyze the slip data on sections of the fault that are short compared to the expected rupture length and along its segments only with no inclusion of the step-over areas. Large paleoearthquakes on the Hope Fault are taken to have reached magnitudes up to $M_w$~7 and hence to have broken lengths of several tens of kilometers. Therefore, as the 30 km section that we analyze is divided into 11 small-scale segments, we first analyze the slip data separately along each of these short segments, outside of the step-over zones that separate them.

Second, to analyze a dense collection of data with variable qualities, values, and uncertainties, we must adopt a probabilistic and statistical approach [e.g., *Scharer et al.*, 2014] and treat separately the different quality data subsets. The physical function that describes the distribution of uncertainties about an offset measurement is unknown. Therefore, one has to make reasonable assumptions on how to best represent this distribution. A classical way is to suppose a continuous probability distribution in which the actual offset has a greater probability to be close to a preferred value and a decreasing probability to be at some distance from this value. The normal or Gaussian distribution is one classical way to represent this continuum. Asymmetric triangular functions have been also proposed [e.g., *Zielke and Arrowsmith*, 2012]. Following many prior works [e.g., *McGill and Sieh*, 1991; *Lowell*, 1995; *McGill and Rubin*, 1999; *Zielke et al.*, 2012; *Beauprêtre et al.*, 2012, 2013; *Benedetti et al.*, 2013; *Scharer et al.*, 2014], we favor the Gaussian representation (referred to as Gaussian probability density function or PDF). In this representation, each measured offset value is the center of a Gaussian individual PDF, whose 2σ width is the largest uncertainty on the measurement. The height over width ratio of an individual PDF thus depends strongly on the uncertainty on the data; the larger the uncertainty, the smaller the ratio and hence the less significant the data within the entire collection. Summing the individual PDFs forms a cumulative offset probability distribution or COPD curve (as defined in *Zielke et al.* [2010]), whose dominant "peaks" indicate the most frequent and/or the most precise values within the entire data collection. Best constrained offset values can thus be clearly

**Table 2.** Best Constrained Lateral Cumulative Offsets (COPD Values) Measured Along Each A to K Segment, Discriminated From Their Quality (Q1: Quality 1, Q2: Quality 2, and Q3: Quality 3)[a]

| Segment A | | | Segment B | | | Segment C | | | Segment D | | | Segment E+F | | | Segment G | | | Segment H | | | Segment I | | | Segment J+K | | | Mean Offset Values (m) |
|---|---|---|---|---|---|---|---|---|---|---|---|---|---|---|---|---|---|---|---|---|---|---|---|---|---|---|---|
| Q1 | Q2 | Q3 | Q1 | Q2 | Q3 | Q1 | Q2 | Q3 | Q1 | Q2 | Q3 | Q1 | Q2 | Q3 | Q1 | Q2 | Q3 | Q1 | Q2 | Q3 | Q1 | Q2 | Q3 | Q1 | Q2 | Q3 | |
| 4,3 | 3,8 | | | | **3** | | 3,5 | **4,3** | **4,5** | 4,2 | 5,4 | | 4,4 | 2,5 | 3,9 | 4,5 | 3,4 | | | | | 3,7 | | | | **3,3** | **4,0** |
| | 6,4 | | | | 7,4 | | | | | | | | | 7 | | | | | | | | | 7,3 | | | | 7,0 |
| 9,3 | | 8,1 | | **8,3** | | | | **8** | 9,1 | | | 8,7 | | | | | 8,2 | | | 9 | | **9,1** | 9,4 | | | | **8,7** |
| | | | | | | | | | | | **11,5** | | | | | | 10,8 | | | | | | | | | | |
| | 13,8 | | | | 13,7 | | **14,4** | 15,6 | 14,7 | | | | 14,7 | | | 14,2 | **14** | 14,4 | 13,4 | 13,7 | 14,4 | | | | | 14 | **14,2** |
| | 18 | 18,8 | | 17,1 | **18,4** | | | 18,9 | | | | | | | | 19 | 18,5 | 18,5 | 17,5 | | 18,5 | | 18 | | | | **18,3** |
| | | 22,2 | | | 22,3 | | 23,6 | | | | | | | | | | 23 | | | | | | | | | | 22,8 |
| | | 27,5 | | | | | | | | | | 28 | | 28,8 | 28 | | | | | | | | | | | | 28,1 |
| | 30,5 | | | | 31 | | | 31,5 | | | | | | | | 29,8 | **29,7** | | | | | | | | 29,9 | | 30,4 |
| | | | | | | | | | | | | | | | | 35,3 | | | | | | | | | 36,8 | | |
| | 43 | | | | | | | | | | | | | | | | 43,5 | | | | | | | | | | |
| 46 | | | | | | | | | | | | | | | | | | | | | | | | | | | |
| | | | | | | | | | | | | | | | | | **48,5** | | | | | | | | | | |
| | | 51 | | | | | | | | | | | | | | | | | | | | | | | | | |
| | | | | | | | | | | | | | | | | | | | | | | | 53 | | | | |
| | | 56,7 | 56 | | | | | | | | | | | | | 55,6 | | | | | | | | | | | 56,1 |
| | | | | | | | | | | | | | | 63 | | | | | | | | | | | | | |
| | | | | | 65 | | | | | | | | | | | | | | | | | | | | | | |
| 67 | | | | | | | | | | | | | | | | | | | | | | | | | | | |
| | | | | | | | | | | | | | | 69 | | | | | | | | | | | | | |
| | | 70 | | | | | | | | | | | | | | | | | | | | | | | | | |

[a]Offsets are derived from the peaks of the COPD curves in Figure S3 in the supporting information. They are limited here to the range of 0–70 m. The COPD values indicated in bold in the A to J + K columns are those constrained by several offset measurements. The COPD values have been aligned according to their similarity among the different segments (this qualitative grouping is statistically refined in Figure 5), and the average offset value is indicated in the last column, calculated for the offsets represented on at least three different segments. These average values are in bold when the offset value is represented on more than four different segments.
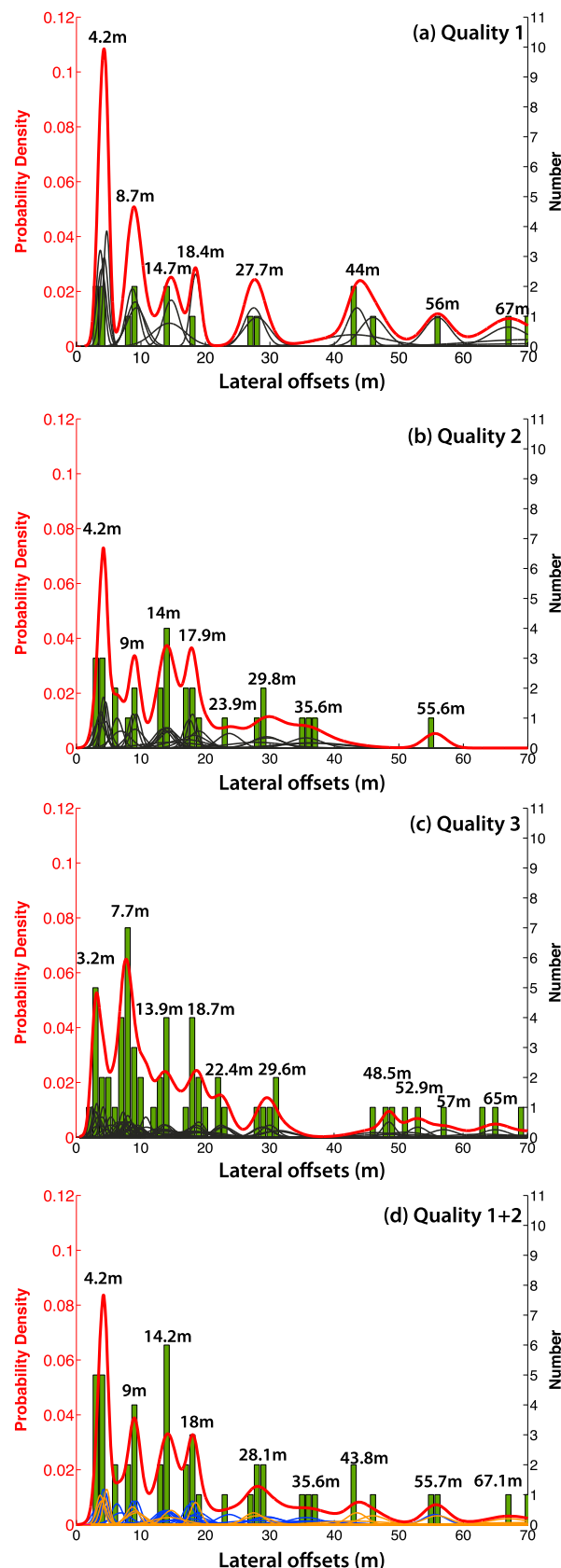
extracted. In the following, we call COPD values the best constrained cumulative offset values derived from the peaks in the COPD plots. There is no simple way to establish the link between the height of a peak in a COPD curve and its "robustness"; this height depends both on the number of data contributing to the peak and on the uncertainty on each of these data. However, the higher and narrower is a peak in a COPD curve, the better defined and/or represented is its value.

In the following, we analyze separately the quality 1, quality 2, and quality 3 data subsets so that their respective potential to record past fault slips can be compared.

### 5.2. Segment Analysis

Each segment (or couple of segments for E–F and J–K) holds 8 to 23 offset measurements of different qualities (Table S2 in the supporting information). As the number of measurements is few in each quality class, especially in the quality 1 class, the peaks in the COPD plots are generally defined from one or a few offsets only (Figure S3 in the supporting information). The COPD values that are derived from two or more offset measurements on a segment, and hence that are better constrained, are indicated in bold in Table 2 (columns A to J + K). This shows that three cumulative offset amounts —about 4 m, 8–9 m, and ~14 m—are well preserved on different segments (Table 2). This is supported by these specific offsets being also revealed in isolated quality 1 and quality 2 measurements. More generally, on each segment, several of the COPD values are revealed in more than one quality

**Figure 5.** Statistical analysis of the entire lateral offset collection in the range of 0–70 m (Table S2 in the supporting information; entire data set shown in Figure S4 in the supporting information). (a–c) The three quality data subsets are analyzed separately, (d) whereas the quality 1 and quality 2 offsets are analyzed together. Each figure compares the histogram of the measurements (in green), the individual PDFs (in black in Figures 5c and in orange for quality 1 data and in blue for quality 2 data in Figure 5d), and the summed PDF curve or COPD plot (in red). The best constrained peak offset values (COPD values) are indicated above the peaks, and are reported in Table 3, along with their uncertainties. See text for details.

**Table 3.** Best Constrained Cumulative Lateral Offsets (COPD Values) and Slip Increments Determined for the Entire Offset Population (Offsets Considered in the Range 0–70 m; Entire Data Set Shown in Figure S4 in the Supporting Information)[a]

| Quality 1 | | Quality2 | | Quality3 | | Quality1 + 2 | |
|---|---|---|---|---|---|---|---|
| COPD (m) | Error (m) | COPD (m) | Error (m) | COPD (m) | Error (m) | COPD (m) | Error (m) |
| **4,2** | 1 | **4,2** | 1,2 | **3,2** | 1 | **4,2** | 1,2 |
| **8,7** | 1,2 | **9** | 1 | **7,7** | 1,2 | **9** | 1 |
| **14,7** | 1 | **14** | 1 | **13,9** | 1 | **14,2** | 1,2 |
| **18,4** | 1,6 | **17,9** | 1 | **18,7** | 1 | **18** | 1 |
|  |  | 23,9 | 3,5 | **22,4** | 1,4 |  |  |
| **27,7** | 1,7 | **29,8** | 1,7 | **29,6** | 1,7 | **28,1** | 1,7 |
|  |  | 35,6 | 3,5 |  |  | 35,6 | 3,5 |
| **44** | 2,6 |  |  |  |  | **43,8** | 2,2 |
|  |  |  |  | 48,5 | 1 |  |  |
|  |  |  |  | 52,9 | 3 |  |  |
| **56** | 4 | 55,6 | 3,5 | 57 | 4 | **55,7** | 1,6 |
| **67** | 6 |  |  | **65** | 2 | **67,1** | 2,8 |
| Slip increments (m) | Error (m) | Slip increments (m) | Error (m) | Slip increments (m) | Error (m) | Slip increments (m) | Error (m) |
| 4,2 | 1,0 | 4,2 | 1,2 | 3,2 | 1,0 | **4,2** | 1,2 |
| 4,5 | 1,6 | 4,8 | 1,6 | 4,5 | 1,6 | **4,8** | 1,6 |
| 6 | 1,6 | 5 | 1,4 | 6,2 | 1,6 | **5,2** | 1,6 |
| 3,7 | 1,9 | 3,9 | 1,4 | 4,8 | 1,4 | **3,8** | 1,6 |
| 9,3 | 2,3 | 6 | 3,6 | 3,7 | 1,7 | **10,1** | 2,0 |
| 16,3 | 3,1 | 5,9 | 3,9 | 7,2 | 2,2 | **7,5** | 3,9 |
| 12 | 4,8 | 5,8 | 3,9 | 18,9 | 2,0 | **8,2** | 4,1 |
| 11 | 7,2 | 20 | 4,9 | 4,4 | 3,2 | **11,9** | 2,7 |
|  |  |  |  | 4,1 | 5,0 | **11,4** | 3,2 |
|  |  |  |  | 8 | 4,5 |  |  |

[a]The three quality data subsets are analyzed separately, and the combined quality 1 and 2 data sets is also analyzed. The COPD values are derived from the peaks of the COPD curves in Figure 5. The COPD values indicated in bold are the best constrained. The 1σ uncertainties on the COPD offsets are indicated (see text for their calculation). The "slip increments" are the amounts of slip that separate the successive COPD values. Their error is calculated as explained in the text. Their analysis is performed in Figure 7.

subset (Table 2). Two evidences arise from these observations. First, similar offsets are found in the different quality measurements performed on each of the segments. Second, those several time-measured offset values are found on distant segments along the fault. In Table 2, we have aligned the COPD values that appear most similar among the segments (this qualitative gathering will be statistically refined in the following section). This confirms that similar offsets are found on different segments along the fault section. Four average offset values are found on more than four different segments (in bold in last column of Table 2), namely, ~4 m (on all segments but H), ~9 m (on all segments but J + K), ~14 m (on all segments), and ~18 m (on all segments but D, E + F, and J + K). Five other average offset values are found on three to four distinct segments, ~7 m (on segments A, B, E + F, and I), ~23 m (on segments A, B, C, and G), ~28 m (on segments B, E + F, and G), ~30 m (on segments B, C, G, and J + K), and ~56 m (on segments A, C, and G). The redundancy of the above nine offset values on a significant number of distant segments attests that these cumulative offsets are well preserved in the morphology. In particular, a common, smallest cumulative offset is found on all segments but H, in the range of 3.5–4.5 m (quality 1 and 2 subsets). Finally, the average common offsets listed above are all separated by a similar slip amount, in the range of 3–5 m (except between ~28 and 30 m and between ~30 and 56 m).

### 5.3. Total Population Analysis

The finding of slip values being in the same narrow ranges at distant points along the fault suggests the fair constancy of the slips (in each specific range) along the fault section. This constancy of the slips along strike permits to analyze together the entire offset collection.

Figure 5 shows the COPD curve for each of the quality 1, quality 2, and quality 3 offset populations and for the combined quality 1 and 2 population (limited to offset range 0–70 m; entire range of values in Figure S4 in the supporting information). COPD values are reported in Table 3, along with their uncertainties. As, generally, there is no simple mathematical function that describes a summed PDF peak, we take the uncertainty on a
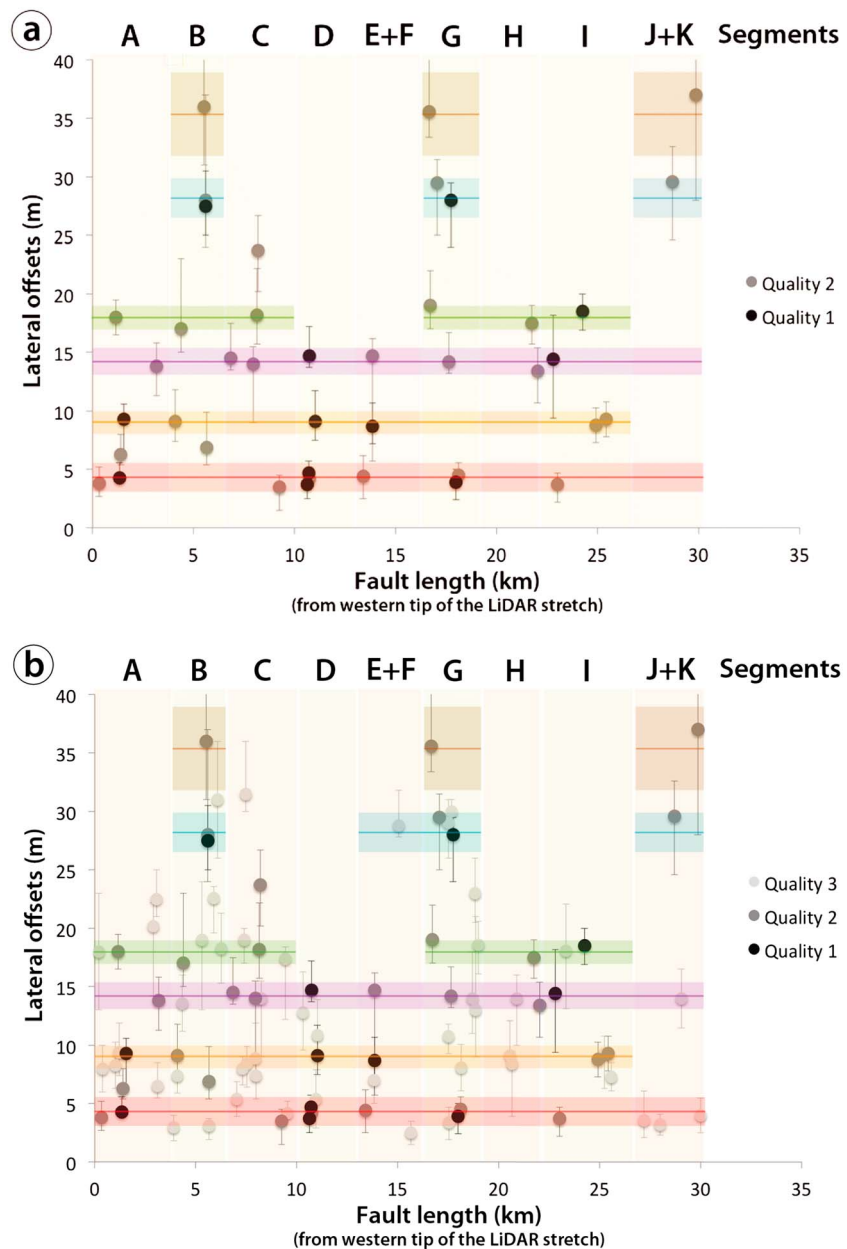
**Figure 6.** Distribution of the measured lateral offsets along the analyzed fault section (offsets limited to the range 0–40 m; all offsets shown in Figure S5 in the supporting information). Zero is taken at the western tip of the lidar stretch. The three data qualities are discriminated with different gray tones. The A–K segments are distinguished with colored vertical bars. The horizontal colored bars represent the COPD values and their uncertainties determined for the quality 1 and 2 data sets (Table 3). (a) Quality 1 and 2 offsets. (b) Quality 1, 2, and 3 offsets. See text for more details.

COPD value equal to the half-width (1σ) of the Gaussian that best approximates the peak shape. In the cases where the COPD peak results (or mainly results) from a single measurement, the uncertainty on the COPD value is that on the measurement.

The COPD curve for the quality 1 population (Figure 5a) exhibits eight peaks, among which two are more pronounced, at $4.2 \pm 1$ and $8.7 \pm 1.2$ m (Table 3). These two offset values are constrained by several (≥3), well-defined measurements, and hence are well preserved in the morphology. Three other COPD values, at $14.7 \pm 1$, $27.7 \pm 1.7$, and $44.0 \pm 2.6$ m, are constrained by at least two well-defined measurements, suggesting that these three cumulative offsets are also well preserved in the morphology. Finally, three other COPD values
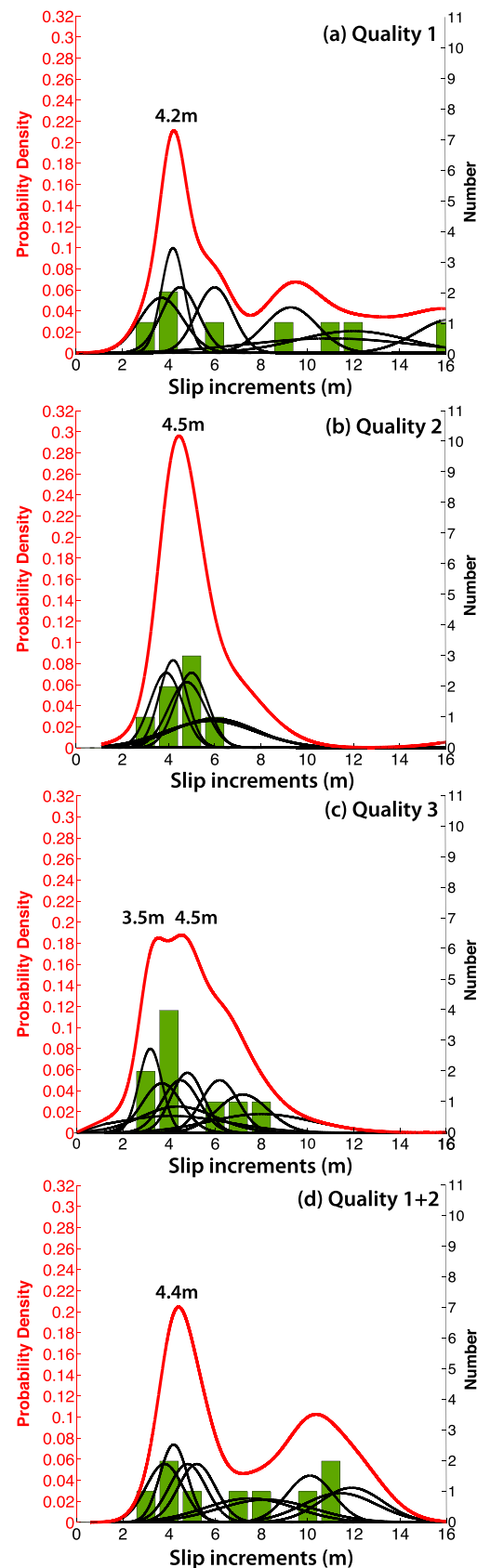
are defined from one single measurement, at $18.4 \pm 1.6$, $56.0 \pm 4$, and $67.0 \pm 6$ m (Table 3). Whereas the two largest offsets are poorly constrained (large uncertainties on the measurements), the $18.4 \pm 1.6$ m cumulative offset is defined from a well-constrained measurement and hence is likely robust.

The COPD curve for the quality 2 population (Figure 5b) shows four pronounced peaks which attest that four cumulative offset values, at $4.2 \pm 1.2$, $9.0 \pm 1$, $14.0 \pm 1$, and $17.9 \pm 1$ m (Table 3), are well preserved and constrained by multiple measurements ($\geq 3$). Four other small peaks are observed, among which two, with offsets of $29.8 \pm 1.7$ and $35.6 \pm 3.5$ m, are derived from three measurements. This suggests that the two latter offsets are meaningful. Finally, the two other small peaks, at $23.9 \pm 3.5$ and $55.6 \pm 3.5$ m, are poorly constrained (Table 3).

The populations of good and moderate quality offsets have thus recorded similarly the four smallest offsets of about 4, 9, 14, and 18 m (see Table 3, where the COPD values of the three data subsets are compared). One larger cumulative offset of 28–30 m is also found in the two data subsets, whereas another large offset of 55–56 m is suggested with a low peak in the two data groups. The comparison of quality 1 and quality 2 records therefore shows that the quality 2 data subset contains the same information on the most recent fault slips (i.e., $\leq$~30 m) as the best constrained quality 1 population. Furthermore, although larger offsets are more poorly preserved, their record is fairly similar in the two data subsets. Therefore, quality 1 and quality 2 measurements can be analyzed collectively. The global COPD curve (Figure 5d) confirms that five cumulative offsets are well preserved in the morphology, of $4.2 \pm 1.2$, $9.0 \pm 1$, $14.2 \pm 1.2$, $18.0 \pm 1$, and $28.1 \pm 1.7$ m, whereas four additional cumulative offsets, of $35.6 \pm 3.5$, $43.8 \pm 2.2$, $55.7 \pm 1.6$, and $67.1 \pm 2.8$ m, seem to be still partially preserved (Table 3). The smallest offset that we find is in good agreement with the smallest offsets that have been reported in prior works (Table S1 in the supporting information).

**Figure 7.** Statistical analysis of the slip increments that separate the COPD values for the (a–c) three data subsets and for the (d) quality 1 and 2 data groups (from Table 3). For clarity, the slip increments are represented in the range of 0–16 m. Each slip increment is represented as a Gaussian PDF (in black). The histogram of the slip increment values is shown in green. The peaks in the COPD plot (in red) indicate the most represented slip increments, whose values are indicated above the peaks (and in Table 3). One common value of incremental slip is found in the three data subsets, of about 4.2–4.5 m. See text for discussion.

Figure 5c provides further insight on the fault slip record. Although the offsets rated as quality 3 are of poor quality, when analyzed collectively with a statistical approach, they reveal information on the past fault slips. Four pronounced peaks are shown in the COPD curve, which reveal preserved cumulative offsets whose amounts are similar within uncertainties to those revealed in the quality 1 and quality 2 subsets: $3.2 \pm 1.0$ m to be compared with $4.2 \pm 1.2$ m, $7.7 \pm 1.2$ m to be compared with $9.0 \pm 1.0$ m, $13.9 \pm 1.0$ m to be compared with $14.2 \pm 1.2$ m, and $18.7 \pm 1.0$ m to be compared with $18.0 \pm 1.0$ m. Two additional peaks are relatively clear, which suggest the record of two larger offsets of $22.4 \pm 1.4$ and $29.6 \pm 1.7$ m. These two larger offsets are also similar within uncertainties to some of the offsets revealed in the quality 1 and quality 2 data subsets ($23.9 \pm 3.5$ m recorded in quality 2 subset and $28.1 \pm 1.7$ m recorded in both quality 1 and 2 subsets). Finally, four larger offsets are suggested with very low COPD peaks. Although these larger offsets are constrained from a few measurements only, it is noteworthy that two of them are similar within uncertainties to offset amounts revealed in the quality 1 and quality 2 subsets: $57 \pm 4$ m to be compared with $55.7 \pm 1.6$ m and $65.0 \pm 2.0$ m to be compared with $67.1 \pm 2.8$ m. Therefore, the slip record preserved in the quality 3 data is fairly similar, overall, to the slip record revealed in the best quality data.

The distribution of the individual offset measurements along the analyzed fault section is shown in Figure 6 (limited to the range of 0–40 m for clarity; all data reported in Figure S5 in the supporting information). The COPD values found for the entire population of quality 1 and 2 data (Table 3) are shown with their uncertainties as colored horizontal bars. With only a few exceptions, each individual measurement of quality 1 or 2 appears similar within uncertainties to a unique COPD value (Figure 6a). Although the graph is noisier when the quality 3 data are included (Figure 6b), most measurements still appear similar within uncertainties to a single COPD value. This confirms that the best offsets determined from the entire data population well represent the local measurements. This in turn suggests that the along-strike-slip variability is low in each specific slip range (i.e., each colored bar in Figure 6).

Table 3 reports the incremental slips that separate the successive COPD values, along with their uncertainties, for the three data subsets and for the combined quality 1 and quality 2 population. Uncertainties on the slip increments are calculated from propagating the errors on the two corresponding COPD values ($\sigma = $ sqrt $[\sigma_1^2 + \sigma_2^2]$ [*Bevington and Robinson*, 2002]). Figure 7 shows the slip increments as individual PDFs (and histogram), along with their COPD curve, for each data group. In each data subset, the majority of the incremental slip values are similar, on the order of $4.2 + 1.3/-0.9$ m in the quality 1 subset (50% of the increment population), $4.5 + 1.8/-1.0$ m in the quality 2 subset (87% of the increment population), and $4.5 + 2.0/-1.4$ m in the quality 3 subset (90% of the increment population). A similar incremental slip amount is thus repeated several times in each data subset, whereas that incremental slip amount is found in the three data subsets. Furthermore, that incremental slip is similar to the smallest and hence the most recent offset recorded on the fault. We might note that two additional incremental slips are suggested in the combined quality 1 and 2 subsets, around 7.5 m (not seen in COPD curve but seen in histogram) and $10.4 + 1.7/-1.1$ m, but they are derived from a few values only.

## 6. Discussion

### 6.1. Morphological Preservation of the Fault Slip Record

The present study was mostly dedicated to examine the fault offset preservation potential of the morphology in a context of high alluvial and tectonic dynamics. Prior field studies on the eastern Hope Fault already showed that the morphology is preserving remnants of past fault slips at local sites along the fault (Table S1 in the supporting information, and references therein). Yet the question remains of whether a richer information might be preserved, that could be valuable to recover the largest amplitudes of slip and the slip-length distributions of the most recent large paleoearthquakes on the fault. To address this question, we have conducted our study in a fault zone where the conditions listed as 1, 2, and 4 in the introduction are fully met.

Concerning the first condition, the identification of more than 200 laterally offset markers in the analyzed fault zone demonstrates the widespread existence of landforms that have recorded the fault displacements. Furthermore, these offset landforms are fairly evenly distributed along the fault (Figure 6 and Figure S5 in the supporting information), offering the potential for a spatially dense slip record.

Concerning the second point, the available geological and geochronological data show that the vast majority of the identified offset markers are of Holocene age (see section 3.3). Furthermore, we found that most fault offsets (COPD values) smaller than ~60 m were recorded by distinct markers that formed at different locations along the fault (Figure 6 and Figure S5 in the supporting information). If the preserved cumulative offsets reflect the major fault slip events (Discussion in next section), we infer that different markers formed during the short periods of time that separated the slip events (one to a few interseismic time spans). Therefore, the marker archive seems to have recorded fairly "continuously" the successive coseismic slips that were produced by the large paleoearthquakes on the fault.

Concerning condition 4, we have analyzed at high resolution a 30 km long stretch of the eastern Hope Fault, thereby long enough to provide a rich slip record, which in turn allows examining the possible along-strike variability of the paleoearthquake slips.

The existence, frequency, completeness, and richness of the offset record being satisfied, the question arises of its fidelity and robustness in regard with the actual fault slip events (point 3 in the Introduction). The question is especially posed since we are analyzing a drainage system that continuously had to adjust to changing conditions as geomorphic and tectonic processes were going on at fast rates [*Bull*, 1991].

When observed collectively, the fault slip record shows a completeness decreasing with time: whether the best quality (Figures 5a, 5b, and 5d) or the lower quality (Figure 5c) offsets are concerned, the envelope curve that would best represent the COPD function resembles an exponential decay that vanishes around 150 m (Figure S4 in the supporting information) and around 70 m for the best preserved offsets (Figure 5). However, because the present study focuses on small offsets, we do not have a clear vision of the preservation of the larger offsets. Nevertheless, our results suggest that the morphological record of the smallest fault slips has degraded over a time period that encompassed approximately 60–70 m of lateral slip. Knowing that the eastern Hope Fault has been slipping over the Holocene at ~23 mm/yr [e.g., *Langridge and Berryman*, 2005, and references therein], we may grossly expect this time to be a few thousands of years.

The preservation of the fault slip record is thus variable. The four most recent slip events (total offsets ≤~20 m; Figure 6 and discussion in next section) are still well preserved in the morphology; even though the quality 2 and, above all, the quality 3 offsets look more degraded than the quality 1 well-preserved offsets, they all retain a similar record of the four most recent events. There are small differences in the COPD values but the offset amounts are similar within uncertainties (Figure 5 and Table 3). Therefore, the quality 3 offsets in the range of 0–20 m are less degraded than they seem to be.

The morphology is also well preserving a few lateral offsets greater than ~20 m. Four similar COPD values are revealed in two or three data subsets (~23 m in quality 2 and 3 subsets; 28–30 m in quality 1, 2, and 3 subsets; 56–57 m in quality 1, 2, and 3 subsets; and ~65–67 m in quality 1 and 3 subsets), whereas one more displacement value is revealed in the best quality data (~44 m in quality 1 subset). Altogether, this suggests that these five slip values are meaningful.

Therefore, in a region of high alluvial and tectonic dynamics as that of the eastern Hope Fault, the morphology preserves a memory of the prehistorical fault slips that is richer than it has been shown so far. Not only slip remnants exist at local sites along the fault as shown in prior works (Table S1 in the supporting information, and references therein) but the morphology also stores a more complete information that constrains the earthquake slip amplitudes and slip-length distributions (discussion in next section). This more complete information could be recovered because airborne lidar data allowed the morphology to be analyzed at high resolution and continuously over a long section of the fault. This led to markedly increase the number of offset measures. Such a great density of measurements is necessary to conduct a statistical analysis that reveals the well-preserved lateral offsets.

### 6.2. Paleoearthquake Slip Amplitudes and Distributions Inferred From the Global Data Set

Here we discuss the coseismic slip amplitudes and slip-length distributions that we infer in the lidar stretch from the global data set. In the following section, we will examine whether alternative slip-length distributions may be viable.

As aseismic slip has not been evidenced on the Hope Fault [*Wallace et al.*, 2007], the cumulative offsets revealed in the present study basically result from the addition of a variable number of coseismic slips, increasing with the age of the recording marker. Note that, in the term "coseismic slip," we include any possible postseismic slip contribution since the two components cannot be discriminated.

While many sizes of earthquakes might produce slip at the ground surface (surface-breaking earthquakes have generally a magnitude ≥~6, however [e.g., *Wells and Coppersmith*, 1994]), only the largest ones produce a slip sufficiently large (≥1–2 m) to be discriminated within measurement uncertainties. Our data therefore only provide information on the largest prehistorical earthquakes on the fault. The number of earthquakes that we might infer is thus necessarily a minimum value, since small earthquakes, undetected in the data, might have also broken the fault. In the case of the Hope Fault however, it has been shown that strain release essentially occurs during large-magnitude ($M_w \geq 7$) earthquakes [e.g., *Langridge et al.*, 2013], whereas small to moderate earthquakes on the fault are few (e.g., http://www.geonet.org.nz). Together, these suggest that the slip increments that separate the COPD values (recovered on each segment or recovered for the entire data set) are a fair estimate of the coseismic slips that were produced by the large paleoearthquakes on the fault, at the site of study.

In the analysis of the entire data set, we found that, in all quality data subsets, most COPD values are separated by a similar amount of incremental slip, averaging $4.4 + 1.0/-0.9$ m (when calculated for the combined quality 1 and 2 population). This ~$4.4 \pm 1.0$ m slip increment is similar to the slip produced by the most recent large earthquake on the fault ($4.2 \pm 1.2$ m; Figure 5d and Table 3). It is found separating different offset values (50, 87, and 90% of the COPD offsets for the quality 1, quality 2, and quality 3 subsets, respectively; see section 5.3), not all in succession (Table 3), which have thus recorded a variable number of earthquakes over different times. Therefore, we interpret this about 4 m slip increment to represent the coseismic slip that was produced by most of the large paleoearthquakes on the eastern Hope Fault. This interpretation implies that large earthquakes on the eastern Hope Fault have been fairly characteristic in terms of surface slip amplitude, at the site of study. This does not mean that they all produced the exact same slip at the surface, but they produced a slip of the same order at the site of study.

Two other incremental slips are suggested in the combined quality 1 and 2 population, around $7.5 \pm 2$ and $10.4 + 1.7/-1.1$ m (Figure 7d). Although they are more poorly constrained, these two slip increments might be viewed as approximate multiples of the smallest incremental slip value (2 and 3 times, respectively). This supports the suggestion that large prehistorical earthquakes on the eastern Hope Fault might have produced a characteristic surface slip of $4.4 \pm 1$ m at the site of study, at least in the last few kiloyears.

If large earthquakes have been characteristic as suggested above, we infer that the four smallest cumulative offsets well preserved in the morphology are the signature of the four most recent large earthquakes on the fault. The quality 1 best constrained measures, as the combined quality 1 and 2 population, reveal the record of up to ~44 m, and possibly ~67 m, of cumulative lateral fault slip. This might suggest that about 10 large earthquakes, and possibly up to 15, have occurred repeatedly in the prehistorical time to produce the measured cumulative offsets.

The quasi-constancy of the slips (in each specific range) along the 30 km section of the fault suggests that at least each of the four most recent large earthquakes produced a fairly "flat" slip-length distribution in the analyzed fault stretch, well represented by one or other of the horizontal colored bars in Figure 6.

### 6.3. Additional Constraints on Rupture Slips and Lengths

A set of independent information provides additional constraints to determine the slip amplitudes, the slip-length distributions, and the rupture lengths of the paleoearthquakes identified in the lidar data:

1. It has been shown that strike-slip ruptures do not propagate across step-overs larger than ~4 km [*Lettis et al.*, 2002; *Wesnousky*, 2006; *Duan and Oglesby*, 2006]. The central Hanmer pull-apart is 6–7 km wide [e.g., *Wood et al.*, 1994], and therefore, it is unlikely that an earthquake rupture on the eastern Hope Fault can cross it. We note that the 1888 North Canterbury earthquake rupture on the western Hope Fault stopped at the Hanmer basin [*Cowan*, 1990, 1991]. Therefore, it is expected that the longest ruptures on the eastern Hope Fault cannot exceed its total length, ~100 km and possibly up to ~120 km (considering the offshore continuation of the fault described by *Barnes and Audru* [1999a, 1999b]).

2. It has been shown that, independent of their slip mode, magnitude ($M_w \geq 6$), context, etc., earthquake slip-length distributions have a generic envelope shape that is triangular and asymmetric [*Manighetti et al.*, 2005; *Wesnousky*, 2008] (Figure S6 in the supporting information [*Manighetti et al.*, 2001, 2005]). Therefore, the coseismic slip gradually tapers over most of the rupture length from a maximum value near one rupture end down to zero at the other rupture extremity.

3. It has been shown that earthquake maximum slip and length are related through scaling functions (most recent empirical scaling functions shown in Figure S7 in the supporting information [*Manighetti et al.*, 2007]). Furthermore, the earthquake maximum slip-length ratio (i.e., proxy of earthquake stress drop) depends on the structural maturity of the ruptured geological fault [e.g., *Kanamori and Anderson*, 1975; *Scholz et al.*, 1986; *Cao and Aki*, 1986; *Anderson et al.*, 1996; *Stirling et al.*, 1996; *Cowan et al.*, 1996; *Manighetti et al.*, 2007] (Figure S7 in the supporting information). As the Hope Fault has been recognized to be a fairly mature fault [e.g., *Cowan et al.*, 1996; *Khajavi et al.*, 2014], it is expected that the slip-length parameters of its earthquakes are well described by the scaling functions of fairly mature faults (functions 3 or 4 in Figure S7 in the supporting information). Said differently, the Hope Fault is expected to produce relatively low stress drop earthquakes.

In Figure S8a in the supporting information, we examine slip-length functions that might be drawn from individual offset measures. We recall that we found similar slip sequences on most A to J-K segments. These sequences are characterized by a smallest offset of about 4 m, then by a series of offsets, the majority of which are also separated by about 4 m (Table 2). Earthquake slip has thus mainly recurred on each segment in multiples of about 4 m. If the ubiquitous ~4 m slip increment is considered as a maximum coseismic slip amplitude, the information from point (iii) suggests that this ~4 m slip has been produced by a rupture whose minimum length must have been ~100 km (function 3 of Figure S7 in the supporting information). We note that such an ~100 km rupture length is in good agreement with the information from point (i). An ~100 km rupture length makes very unlikely the scenarios 1 and 3 in Figure S8a in the supporting information (more details in figure caption). Only scenario 2 is viable, and it is actually the one we described in section 6.2. In this scenario 2, because the coseismic slip must taper gradually from ~4 m in the lidar stretch down to zero at one rupture end (information from point (ii)), it is expected that slip tapers eastward, for the close proximity (~15 km) of the Hanmer pull-apart to the west prevents gentle westward slip tapering (Figure S8b in the supporting information). Rather, earthquake slip arrest is expected at the Hanmer basin, and therefore, a high slip gradient might be anticipated over the ~15 km that separate the lidar stretch from the Hanmer basin (Figure S8b in the supporting information).

Conversely, if the ubiquitous ~4 m slip increment is lower than the actual maximum coseismic slip, information from point (i) (i.e., rupture length of 100–120 km) suggests that the actual maximum slip amplitude cannot be larger than ~5.5 m (Figure S7 in the supporting information). This makes very unlikely scenarios 5 to 8 in Figure S8a in the supporting information (more details in figure caption). Only the scenarios referred to as 4a and 4b might be viable, provided that the maximum slip outside of the lidar stretch is at most ~5.5 m. These scenarios are actually fairly similar to the scenario 2 described before, since, as scenario 2, they involve similar repeating earthquakes that each produced 4–5 m of coseismic slip in the 30 km lidar stretch, whereas the maximum ~5.5 m coseismic slip is similar within uncertainties to the average 4.4 ± 1.0 m slip that we measured.

We conclude that the slip amplitudes (4.4 ± 1.0 m) and the slip-length distributions described in section 6.2 (Figure 6 and Figure ES8b in the supporting information) are the most likely.

### 6.4. Timing and Magnitudes of the Paleoearthquakes

The morphological approach that we followed does not provide any dating of the identified paleoearthquakes. However, the paleoseismological works that have been conducted on the eastern Hope Fault [*Cowan and McGlone*, 1991; *Bull et al.*, 1994; *Bull and Brandon*, 1998; *Langridge et al.*, 2003, 2013] combine to show the following:

1. Much of the Hope Fault broke during the preceding two centuries (170–360 year ago [*Langridge et al.*, 2013]). At least one and possibly two large earthquakes broke the eastern Hope Fault in that time span. The lateral slips produced by these two recent paleoearthquakes were estimated between ~3 and ~4.9 m [*Langridge et al.*, 2003; *Beauprêtre et al.*, 2012]. These two prehistorical earthquakes might have produced the two smallest cumulative slips that we measured, at 4.2 ± 1.2 m and 9.0 ± 1.0 m (their coseismic slip would thus have been ~4.2 and ~4.8 m, respectively, in agreement with prior suggestions).

2. Much of the Hope Fault failed in at least one or two large earthquakes in the time range of 400–700 years. Although the slips produced by these older paleoearthquakes are not well constrained, amounts up to 5–6 m have been suggested [e.g., *Langridge et al.*, 2013, and references therein]. These one or two large earthquakes might have combined to produce the cumulative slips that we measured at $14.2 \pm 1.2$ m and $18.0 \pm 1.0$ m (their coseismic slip would thus have been ~5.2 and ~3.8 m, respectively, in agreement with prior suggestions).

Assuming that the paleoearthquakes broke the entire length of the eastern Hope Fault, i.e., 100–120 km, and produced a maximum coseismic slip of $4.4 \pm 1$ m at the ground surface (hence a mean slip $D_{mean}$ of $2.2 \pm 0.5$ m; see *Manighetti et al.* [2005] for relationship between maximum and mean coseismic slips), we can estimate their magnitudes, using either the general formula of *Hanks and Kanamori* [1979]; $M_w = 2/3 \log M_0 - 6.0$, with $M_0 = \mu * L * W * D_{mean}$, $\mu = 30.10^9$ Pa and $W$ the seismogenic thickness, here estimated to be 10–14 km [*Leitner et al.*, 2001]) or the regional formula established by *Stirling et al.* [2008] from New Zealand instrumental earthquakes ($M_w = 4.18 + 2/3 \log W + 4/3 \log L$, $W$ the rupture width and $L$ the rupture length, both in kilometer). From the formula of *Hanks and Kanamori* [1979], we find that the paleoearthquakes had a magnitude $M_w$ in the range of 7.1–7.4, whereas the magnitude range is 7.5–7.7 when it is estimated with *Stirling et al.*'s [2008] formula.

These magnitude estimates are minimum values however since coseismic slips measured at surface are generally lower than those produced at depth [e.g., *Manighetti et al.*, 2007, in particular their Figure G in the supporting information].

Our data do not permit discussing the recurrence times of the identified large paleoearthquakes. Indeed, an increasing number of observations show that large earthquakes commonly occur in short temporal clusters [e.g., *Scholz*, 2010; *Schlagenhauf et al.*, 2011; *Benedetti et al.*, 2013, and references therein], and this implies that estimating earthquake recurrence times from cumulative offset to slip rate ratios is likely misleading. Therefore, we can only infer that about 10 and possibly up to ~15 large earthquakes have broken the eastern Hope Fault in the last few thousands of years, each producing about $4.4 \pm 1$ m of lateral slip at the ground surface (at the site of study), and altogether adding to produce between ~44 and 67 m of cumulative lateral displacement on the fault.

## 7. Conclusions

Field studies on active strike-slip faults have shown for decades that the present morphology preserves remnants of prehistorical earthquake slips, even in contexts of high alluvial and tectonic dynamics where landforms are rapidly evolving. However, the measured fault offsets—especially the smallest ones attributed to the most recent paleoearthquakes, are generally few along the faults, so that they rarely allow recovering the slip-length distributions and the largest slips produced by the past earthquakes.

Over the last decade, airborne lidar data have provided an unprecedented tool to remotely analyze and measure the topography at a very high resolution (generally ≤1 m) and continuously over a significant length of a fault, including in vegetated zones where field observations are commonly lacking. Applied to major strike-slip faults in semiarid environments, the lidar and other types of high-resolution remote data have proved to be powerful to identify a large number of well-preserved offset geomorphic landforms that had not been described before and to precisely measure their cumulative offsets [*Zielke et al.*, 2010, 2012; *Klinger et al.*, 2011]. From this dense collection of offset data, the fault slip accumulation patterns could be described, generally for the first time.

Here we analyze airborne lidar data acquired on a 30 km long stretch of a fast-slipping strike-slip fault (eastern Hope Fault, New Zealand) located in a region with highly dynamic alluvial conditions. In these specific conditions, the fault-offset landforms are expected to be rapidly modified and degraded as the alluvial and tectonic processes are going on at fast rates. Field investigations on the eastern Hope Fault confirm that well-preserved lateral offsets are relatively few (10 offsets <60 m; Table S1 in the supporting information). We thus analyzed the lidar data to examine whether, in spite of these complex conditions, the morphology would store valuable information on the prehistorical earthquake slips, that is, information rich enough to recover the slip-length distributions and the largest slips produced by the most recent large earthquakes on the fault.

Our results show that the morphology does contain valuable information on the paleoearthquake slips. Laterally offset landforms are numerous (>200) in the analyzed fault stretch, but most have a complex or a subtle trace, likely because they have been partly degraded over time. It results that only ~30% of these lateral offsets can be measured confidently (rated as quality 1 and quality 2 offsets), whereas ~30% are more uncertain (rated as quality 3 offsets) and ~40% are too complex to be measured (rated as quality 4 offsets). The quality 1 and 2 offsets allow recovering the slip-length distributions and the largest slips of the four most recent large paleoearthquakes on the fault, and they additionally provide evidence of at least 4–6 prior events. This geomorphic record suggests that large earthquake slip recurred in multiples of about 4 m (4.4 ± 1 m on average) along the ~30 km fault stretch. Although it is more complex and hence possibly including some misleading measures, the slip record of the quality 3 offsets reveals a similar information on the past earthquake slips. This shows that past fault slip evidence is stored, not only in well exposed and preserved offsets but also in less clear morphological imprints that have been partially degraded. However, to recover this information, it is necessary that the morphology be analyzed at high resolution (~1 m) and continuously over a long fault stretch (several tens of kilometers), so that a large number of offset landforms can be identified and measured with appropriate uncertainties. A great density of measurements is indeed mandatory to conduct a statistical analysis that can smooth out the possible misleading measures and reveal the robust, well-preserved lateral offsets.

Lidar data provide an unprecedented opportunity to remotely analyze the ground morphology at almost every site of a fault (provided that vegetation is not too dense [see *Langridge et al.*, 2014]) and at a very high resolution (≤1 m). It thus permits a new form of remote-sensing paleoseismology that might help earthquake geologists to recover the fundamental properties of the prehistorical earthquake slips, even in contexts where well-preserved fault offsets seem to be few. This remote paleoseismology can in no way replace fieldwork, but it can prepare it through the prior identification of fault sites with offset landforms and through the remote measurement of these offsets. Fieldwork is then mandatory to validate some of the offset measures and to sample the offset features for dating. For instance, in our study, we provide more than 200 site locations (Table S2 in the supporting information) where a laterally offset landform is identified or suspected, and we also provide 134 offset measurements. Some of these measurements are uncertain (quality 3 and 4) and thus need a field validation. All offsets, with a priority on those of best quality, also need to be dated so as to recover, not only the slip history as we do here but also the time history of the paleoearthquakes. We hope that our work will motivate new studies on the Hope Fault and on other faults in highly dynamic conditions.

**References**

Anderson, J. G., S. G. Wesnousky, and M. W. Stirling (1996), Earthquake size as a function of fault slip rate, *Bull. Seismol. Soc. Am.*, 86(3), 683–690.

Armijo, R., P. Tapponnier, and T. Han (1989), Late Cenozoic right-lateral strike-slip faulting in southern Tibet, *J. Geophys. Res.*, 94(B3), 2787–2838, doi:10.1029/JB094iB03p02787.

Armijo, R., B. Meyer, S. Navarro, G. King, and A. Barka (2002), Asymmetric slip partitioning in the Sea of Marmara pull-apart: A clue to propagation processes of the North Anatolian Fault?, *Terra Nova*, 14(2), 80–86.

Arrowsmith, J. R., and O. Zielke (2009), Tectonic geomorphology of the San Andreas Fault zone from high resolution topography: An example from the Cholame segment, *Geomorphology*, 113, 70–81, doi:10.1016/j.geomorph.2009.01.002.

Barnes, P. M., and J. C. Audru (1999a), Recognition of active strike-slip faulting from high-resolution marine seismic reflection profiles: Eastern Marlborough fault system, New Zealand, *Geol. Soc. Am. Bull.*, 111(4), 538–559.

Barnes, P. M., and J. C. Audru (1999b), Quaternary faulting in the offshore Flaxbourne and Wairarapa basins, southern Cook Strait, New Zealand, *N. Z. J. Geol. Geophys.*, 42(3), 349–367.

Barth, N. C., V. G. Toy, R. M. Langridge, and R. J. Norris (2012), Scale dependence of oblique plate boundary partitioning: New insights from lidar, central Alpine Fault, New Zealand, *Lithosphere*, 4, 435–448, doi:10.1130/L201.1.

Beauprêtre, S., et al. (2012), Finding the buried record of past earthquakes with GPR-based palaeoseismology: A case study on the Hope Fault, New Zealand, *Geophys. J. Int.*, 189(1), 73–100, doi:10.1111/j.1365-246X.2012.05366.x.

Beauprêtre, S., I. Manighetti, S. Garambois, J. Malavieille, and S. Dominguez (2013), Stratigraphic architecture and fault offsets of alluvial terraces at Te Marua, Wellington Fault, New Zealand, revealed by pseudo-3D GPR investigation, *J. Geophys. Res. Solid Earth*, 118, 4564–4585, doi:10.1002/jgrb.50317.

Bell, J. W., F. Amelung, and G. C. King (1997), Preliminary late Quaternary slip history of the Carboneras Fault, southeastern Spain, *J. Geodyn.*, 24(1), 51–66.

Benedetti, L., I. Manighetti, Y. Gaudemer, R. Finkel, J. Malavieille, K. Pou, and ASTER Team (2013), Earthquake synchrony and clustering on Fucino Faults (central Italy) as revealed from in situ [36]Cl exposure dating, *J. Geophys. Res. Solid Earth*, 118, 4948–4974, doi:10.1002/jgrb.50299.

Berryman, K. R., S. Beanland, A. F. Cooper, H. N. Cutten, R. J. Norris, and P. R. Wood (1992), The Alpine Fault, New Zealand: Variation in Quaternary structural style and geomorphic expression, *Ann. Tectonicae*, 6, 126–163.

Berryman, K., A. Cooper, R. Norris, P. Villamor, R. Sutherland, T. Wright, E. Schermer, R. Langridge, and G. Biasi (2012), Late Holocene rupture history of the Alpine Fault in south Westland, New Zealand, *Bull. Seismol. Soc. Am.*, 102(2), 620–638.

Bevington, P. R., and D. K. Robinson (2002), *Data Reduction and Error Analysis for the Physical Sciences*, 3rd ed., McGraw-Hill, New York, ISBN 0-07-119926-8.

Bevis, M., et al. (2005), The B4 project: Scanning the San Andreas and San Jacinto fault zones, Eos Trans. *AGU* 86, no. 52, Fall Meet. Suppl., Abstract H34B-01.

Biasi, G. P., and R. J. Weldon (2006), Estimating surface rupture length and magnitude of paleoearthquakes from point measurements of rupture displacement, *Bull. Seismol. Soc. Am.*, *96*(5), 1612–1623.

Bull, W. B. (1991), *Geomorphic Responses to Climate Change*, Oxford Univ. Press, New York.

Bull, W. B., and M. T. Brandon (1998), Lichen dating of earthquake-generated regional rockfall events, southern Alps, New Zealand, *Geol. Soc. Am. Bull.*, *110*(1), 60–84.

Bull, W. B., J. King, F. Kong, T. Moutoux, and W. M. Phillips (1994), Lichen dating of coseismic landslide hazards in Alpine mountains, *Geomorphology*, *10*, 253–264.

Burbank, D. W., and R. S. Anderson (2011), *Tectonic Geomorphology*, John Wiley, New York.

Cao, T., and K. Aki (1986), Seismicity simulation with a rate- and state-dependent friction law, *Pure Appl. Geophys.*, *124*(3), 487–513.

Cappa, F., C. Perrin, I. Manighetti, and E. Delor (2014), Off-fault long-term damage: A condition to account for generic, triangular earthquake slip profiles, *Geochem., Geophys., Geosyst.*, *15*(4), 1476–1493, doi:10.1002/2013GC005182.

Clayton, L. (1966), Tectonic depressions along the Hope Fault, a transcurrent fault in North Canterbury, New Zealand, *N. Z. J. Geol. Geophys.*, *9*(1–2), 95–104.

Cowan, H. A. (1989), An evaluation of the late Quaternary displacements and seismic hazard associated with the Hope and Kakapo Faults, Amuri District, North Canterbury, MS thesis, Univ. of Canterbury, Christchurch.

Cowan, H. A. (1990), Late Quaternary displacements on the Hope Fault at Glynn Wye, North Canterbury, *N. Z. J. Geol. Geophys.*, *33*, 285–293.

Cowan, H. A. (1991), The North Canterbury earthquake of September 1, 1888, *J. R. Soc. N. Z.*, *21*, 1–12.

Cowan, H. A., and M. S. McGlone (1991), Late Holocene displacements and characteristic earthquakes on the Hope River segment of the Hope Fault, New Zealand, *J. R. Soc. N. Z.*, *21*(4), 285–293.

Cowan, H., A. Nicol, and P. Tonkin (1996), A comparison of historical and paleoseismicity in a newly formed fault zone and a mature fault zone, North Canterbury, New Zealand, *J. Geophys. Res.*, *101*(B3), 6021–6036, doi:10.1029/95JB01588.

Davis, K., D. W. Burbank, D. Fisher, S. Wallace, and D. Nobes (2005), Thrust-fault growth and segment linkage in the active Ostler fault zone, New Zealand, *J. Struct. Geol.*, *27*(8), 1528–1546, doi:10.1016/j.jsg.2005.04.011.

De Pascale, G. P., M. C. Quigley, and T. R. H. Davies (2014), Lidar reveals uniform Alpine Fault offsets and bimodal plate boundary rupture behavior, New Zealand, *Geology*, *42*(5), 411–414, doi:10.1130/G35100.1.

Duan, B., and D. D. Oglesby (2006), Heterogeneous fault stresses from previous earthquakes and the effect on dynamics of parallel strike-slip faults, *J. Geophys. Res.*, *111*, B05205, doi:10.1029/2005JB004138.

Eusden, J. D., J. R. Pettinga, and J. K. Campbell (2000), Structural evolution and landscape development of a collapsed transpressive duplex on the Hope Fault, North Canterbury, New Zealand, *N. Z. J. Geol. Geophys.*, *43*, 391–404.

Eusden, J. D., Jr., J. R. Pettinga, and J. K. Campbell (2005), Structural collapse of a transpressive hanging-wall fault wedge, Charwell region of the Hope Fault, South Island, New Zealand, *N. Z. J. Geol. Geophys.*, *48*(2), 295–309.

Frankel, K. L., J. F. Dolan, R. C. Finkel, L. A. Owen, and J. S. Hoeft (2007), Spatial variations in slip rate along the Death Valley–Fish Lake Valley fault system determined from lidar topographic data and cosmogenic Be-10 geochronology, *Geophys. Res. Lett.*, *34*, L18303, doi:10.1029/2007GL030549.

Freund, R. (1971), The Hope Fault: A strike-slip fault in New Zealand, *N. Z. Geol. Surv. Bull.*, *86*, 49.

Gaudemer, Y., P. Tapponnier, and D. Turcotte (1989), River offsets across active strike-slip faults, *Ann. Tectonicae*, *3*(3), 55–76.

Gaudemer, Y., P. Tapponnier, B. Meyer, G. Peltzer, C. Shunmin, C. Zhitai, D. Huagung, and I. Cifuentes (1995), Partitioning of crustal slip between linked, active faults in the eastern Qilian Shan, and evidence for a major seismic gap, the "Tianzhu gap," on the western Haiyuan Fault, Gansu (China), *Geophys. J. Int.*, *120*, 599–645, doi:10.1111/j.1365-246X.1995.tb01842.x.

Gold, R. D., and E. Cowgill (2011), Deriving fault-slip histories to test for secular variation in slip, with examples from the Kunlun and Awatere Faults, *Earth Planet. Sci. Let.*, *301*(2011), 52–64, doi:10.1016/j.epsl.2010.10.011.

Gold, R., E. Cowgill, J. R. Arrowsmith, X. Chen, W. D. Sharp, K. M. Cooper, and X. F. Wang (2011), Faulted terrace risers place new constraints on the late Quaternary slip rate for the central Altyn Tagh Fault, northwest Tibet, *Geol. Soc. Am. Bull.*, doi:10.1130/B30207.1.

Haddad, D. E., S. O. Akçiz, J. R. Arrowsmith, D. D. Rhodes, J. S. Oldow, O. Zielke, N. A. Toké, A. G. Haddad, J. Mauer, and P. Shilpakar (2012), Applications of airborne and terrestrial laser scanning to paleoseismology, *Geosphere*, *8*(4), 771–786, doi:10.1130/GES00701.1.

Haibing, L., P. Van der Woerd, P. Tapponnier, Y. Klinger, Q. Xuexiang, Y. Jingsui, and Z. Yintang (2005), Slip rate on the Kunlun Fault at Hongshui Gou, and recurrence time of great events comparable to the 14/11/2001, $M_w$~7.9 Kokoxili earthquake, *Earth Planet. Sci. Lett.*, *237*(1), 285–299.

Hanks, T. C., and H. Kanamori (1979), A moment magnitude scale, *J. Geophys. Res.*, *84*, 2348–2350, doi:10.1029/JB084iB05p02348.

Hardy, E. F., and H. W. Wellman (1984), *The Alpine, Wairau and Hope Faults*, Victoria Univ. of Wellington, Geology Department, Wellington, New Zealand.

Haugerud, R., D. J. Harding, S. Y. Johnson, J. L. Harless, C. S. Weaver, and B. L. Sherrod (2003), High-resolution lidar topography of the Puget Lowland, Washington: A bonanza for Earth science, *Geol. Soc. Am.*, *13*(6), 4–9.

Hecker, S., N. A. Abrahamson, and K. E. Wooddell (2013), Variability of displacement at a point: Implications for earthquake-size distribution and rupture hazard on faults, *Bull. Seismol. Soc. Am.*, *103*(2A), 651–674.

Hubert-Ferrari, A., R. Armijo, G. King, B. Meyer, and A. Barka (2002), Morphology, displacement, and slip rates along the North Anatolian Fault, Turkey, *J. Geophys. Res.*, *107*(B10), 2235, doi:10.1029/2001JB000393.

Kanamori, H., and D. L. Anderson (1975), Theoretical basis of some empirical relations in seismology, *Bull. Seismol. Soc. Am.*, *65*(5), 1073–1095.

Khajavi, N., M. Quigley, and R. M. Langridge (2014), Influence of topography and basement depth on surface rupture morphology revealed from lidar and field mapping, Hope Fault, New Zealand, *Tectonophysics*, doi:10.1016/j.tecto.2014.05.032.

Klinger, Y., J. P. Avouac, N. A. Karaki, L. Dorbath, D. Bourles, and J. L. Reyss (2000), Slip rate on the Dead Sea transform fault in northern Araba valley (Jordan), *Geophys. J. Int.*, *142*(3), 755–768.

Klinger, Y., X. Xu, P. Tapponnier, J. Van der Woerd, C. Lasserre, and G. King (2005), High-resolution satellite imagery mapping of the surface rupture and slip distribution of the $M_w$~7.8, 14 November 2001 Kokoxili earthquake, Kunlun Fault, northern Tibet, China, *Bull. Seismol. Soc. Am.*, *95*(5), 1970–1987.

Klinger, Y., M. Etchebes, P. Tapponnier, and C. Narteau (2011), Characteristic slip for five great earthquakes along the Fuyun Fault in China, *Nat. Geosci.*, *4*, 389–392.

Knuepfer, P. L. K. (1984), Tectonic geomorphology and present-day tectonics of the alpine shear system, South Island, New Zealand (Neotectonics, Faults), The Univ. of Arizona.

Knuepfer, P. L. K. (1988), Estimating ages of late Quaternary stream terraces from analysis of weathering rinds and soils, *Geol. Soc. Am. Bull.*, *100*, 1224–1236.

Knuepfer, P. L. K. (1992), Temporal variations in latest Quaternary slip across the Australian-Pacific Plate Boundary, northeastern South Island, New Zealand, *Tectonics*, *11*(3), 449, doi:10.1029/91TC02890.

Kondo, H., S. Toda, K. Okamura, K. Takada, and T. Chiba (2008), A fault scarp in an urban area identified by lidar survey: A case study on the Itoigawa–Shizuoka Tectonic Line, central Japan, *Geomorphology*, *101*, 731–739.

Lacassin, R., A. Replumaz, and P. H. Leloup (1998), Hairpin river loops and slip-sense inversion on southeast Asian strike-slip faults, *Geology*, *26*(8), 703–706.

Langridge, R. M., and K. R. Berryman (2005), Morphology and slip rate of the Hurunui section of the Hope Fault, South Island, New Zealand, *N. Z. J. Geol. Geophys.*, *48*, 43–57.

Langridge, R. M., J. K. Campbell, N. Hill, V. Pere, J. Pope, J. R. Pettinga, B. Estrada, and K. R. Berryman (2003), Paleoseismology and slip rate of the Conway Segment of the Hope Fault at Greenburn Stream, South Island, New Zealand, *Ann. Geophys.*, *46*(5), 1119–1139.

Langridge, R. M., P. C. Almond, and R. P. Duncan (2013), Timing of late Holocene paleoearthquakes on the Hurunui segment of the Hope Fault: Implications for plate boundary strain release through South Island, New Zealand, *Geol. Soc. Am. Bull.*, doi:10.1130/B30674.1.

Langridge, R. M., W. F. Ries, T. Farrier, N. C. Barth, N. Khajavi, and G. P. De Pascale (2014), Developing sub 5 m lidar DEMs for forested sections of the Alpine and Hope Faults, South Island, New Zealand: Implications for structural interpretations, *J. Struct. Geol.*, *64*, 53–66.

Lasserre, C., et al. (1999), Post-glacial left slip-rate and past occurrence of $M \geq 8$ earthquakes on the western Haiyuan Fault (Gansu, China), *J. Geophys. Res.*, *104*, 17,633–17,651, doi:10.1029/1998JB900082.

Leitner, B., D. Eberhart-Phillips, H. Anderson, and J. L. Nabelek (2001), A focused look at the Alpine Fault, New Zealand: Seismicity, focal mechanisms, and stress observations, *J. Geophys. Res.*, *106*(B2), 2193–2220, doi:10.1029/2000JB900303.

Lensen, G. (1968), Analysis of progressive fault displacements during downcutting at the Branch River terraces, South Island, *Geol. Soc. Am. Bull.*, *79*, 545–566.

Lettis, W., J. Bachhuber, R. Witter, C. Brankman, C. E. Randolph, A. Barka, W. D. Page, and A. Kaya (2002), Influence of releasing step-overs on surface fault rupture and fault segmentation: Examples from the 17 August 1999 Izmit earthquake on the North Anatolian Fault, Turkey, *Bull. Seismol. Soc. Am.*, *92*(1), 19–42.

Li, H., J. Van der Woerd, Z. Sun, J. Si, P. Tapponnier, J. Pan, D. Liu, and M. L. Chevalier (2012), Co-seismic and cumulative offsets of the recent earthquakes along the Karakax left-lateral strike-slip fault in western Tibet, *Gondwana Res.*, *21*(1), 64–87.

Lin, Z., H. Kaneda, S. Mukoyama, N. Asada, and T. Chiba (2013), Detection of subtle tectonic–geomorphic features in densely forested mountains by very high-resolution airborne lidar survey, *Geomorphology*, *182*, 104–115.

Little, T. A., and A. Jones (1998), Seven million years of strike-slip and off-fault deformation on the Awatere Fault,South Island, New Zealand, *Tectonics*, *17*, 285–302, doi:10.1029/97TC03148.

Lowell, T. V. (1995), The application of radiocarbon age estimates to the dating of glacial sequences: An example from the Miami sublobe, Ohio, U.S.A, *Quat. Sci. Rev.*, *14*, 85–99.

Manighetti, I., G. C. P. King, Y. Gaudemer, C. H. Scholz, and C. Doubre (2001), Slip accumulation and lateral propagation of active normal faults in Afar, *J. Geophys. Res.*, *106*(B7), 13,667–13,696, doi:10.1029/2000JB900471.

Manighetti, I., M. Campillo, C. Sammis, P. M. Mai, and G. King (2005), Evidence for self-similar, triangular slip distributions on earthquakes: Implications for earthquake and fault mechanics, *J. Geophys. Res.*, *110*, B05302, doi:10.1029/2004JB003174.

Manighetti, I., M. Campillo, S. Bouley, and F. Cotton (2007), Earthquake scaling, fault segmentation, and structural maturity, *Earth Planet. Sci. Lett.*, *253*, 429–438.

Manighetti, I., D. Zigone, M. Campillo, and F. Cotton (2009), Self-similarity of the largest-scale segmentation of the faults: Implications for earthquake behavior, *Earth Planet. Sci. Lett.*, *288*, 370–381, doi:10.1016/j.epsl.2009.09.040.

Manighetti, I., C. Caulet, L. Barros, C. Perrin, F. Cappa, and Y. Gaudemer (2015), Generic along-strike segmentation of Afar normal faults, East Africa: Implications on fault growth and stress heterogeneity on seismogenic fault planes, *Geochem., Geophys., Geosyst.*, *16*, 443–467, doi:10.1002/2014GC005691.

McCalpin, J. P. (Ed.) (1996), *Paleoseismology*, 1st ed., pp. 583, Academic Press, New York.

McCalpin, J. P. (Ed.) (2009), *Paleoseismology*, *Int. Geophys. Ser.*, vol. 95, 2nd ed., pp. 629, Academic Press-Elsevier, New York.

McGill, S. F., and C. F. Rubin (1999), Surficial slip distribution on the central Emerson Fault during the June 28, 1992, Landers earthquake, California, *J. Geophys. Res.*, *104*(B3), 4811–4833, doi:10.1029/98JB01556.

McGill, S. F., and K. Sieh (1991), Surficial Offsets on the central and eastern Garlock Fault associated with prehistoric earthquakes, *J. Geophys. Res.*, *96*(B13), 21,597–21,621, doi:10.1029/91JB02030.

McGlone, M. S. (1988), New Zealand, in *Vegetation History*, edited by B. Huntley and T. Webb III, pp. 557–599, Kluwer Acad., Dordrecht, Netherlands.

McKay, A. (1890), On the earthquakes of September 1888 in the Amuri and Marlborough Districts of the South Island, *New Zealand Geological Survey Report of Geological Explorations* 20, p. 1–16.

McMorran, T. J. (1991), The Hope Fault at Hossack Station east of Hanmer Basin, North Canterbury, MSc thesis, Univ. of Canterbury Library, Christchurch, New Zealand.

Meigs, A. (2013), Active tectonics and lidar revolution, *Lithosphere*, *5*, 226–229, doi:10.1130/RF.L004.1.

Mériaux, A. S., et al. (2005), The Aksay segment of the northern Altyn Tagh Fault: Tectonic geomorphology, landscape evolution, and Holocene slip rate, *J. Geophys. Res.*, *110*, B04404, doi:10.1029/2004JB003210.

Nissen, E., T. Maruyama, J. R. Arrowsmith, J. R. Elliott, A. K. Krishnan, M. E. Oskin, and S. Saripalli (2014), Coseismic fault zone deformation revealed with differential lidar: Examples from Japanese $M_w$~7 intraplate earthquakes, *Earth Planet. Sci. Lett.*, *405*, 244–256.

Oskin, M. E., K. Le, and M. D. Strane (2007), Quantifying fault-zone activity in arid environments with high-resolution topography, *Geophys. Res. Lett.*, *34*, L23S05, doi:10.1029/2007GL031295.

Oskin, M. E., et al. (2012), Near-field deformation from the El Mayor–Cucapah earthquake revealed by differential lidar, *Science*, *335*(6069), 702–705.

Ouchi, S. (2005), Development of offset channels across the San Andreas Fault, *Geomorphology*, *70*(1), 112–128.

Peltzer, G., P. Tapponnier, Y. Gaudemer, B. Meyer, S. Guo, K. Yin, Z. Chen, and H. Dai (1988), Offsets of late Quaternary morphology, rate of slip, and recurrence of large earthquakes on the Chang Ma Fault (Gansu, China), *J. Geophys. Res.*, *93*(B7), 7793–7812, doi:10.1029/JB093iB07p07793.

Pope, J. G. (1994), Secondary structures, Holocene displacements and paleo-seismicity of the Conway Segment of the Hope Fault, Greenburn Stream to Sawyers Creek, BSc thesis, Univ. of Canterbury, Christchurch.

Rattenbury, M. S., D. B. Townsend, and M. R. Johnston (2006), Geology of the Kaikoura Area, Institute of Geological and Nuclear Sciences 1:250000 geological map, 13, 1 sheet +70pp.

Ritz, J. F., E. T. Brown, D. L. Bourles, H. Philip, A. Schlupp, G. M. Raisbeck, F. Yiou, and B. Enkhtuvshin (1995), Slip rates along active faults estimated with cosmic-ray–exposure dates: Application to the Bogd Fault, Gobi-Altaï, Mongolia, *Geology*, *23*(11), 1019–1022.

Rizza, M., S. Mahan, J. F. Ritz, H. Nazari, J. Hollingsworth, and R. Salamati (2011), Using luminescence dating of coarse matrix material to estimate the slip rate of the Astaneh Fault, Iran, *Quat. Geochronology*, *6*(3), 390–406.

Rizza, M., et al. (2015), Earthquake geology of the Bulnay Fault (Mongolia), *Bull. Seismol. Soc. Am.*, *105*(1), 72–93.

Rockwell, T., C. Loughman, and P. Merifield (1990), Late Quaternary rate of slip along the San Jacinto fault zone near Anza, southern California, *J. Geophys. Res.*, *95*(B6), 8593–8605, doi:10.1029/JB095iB06p08593.

Salisbury, J. B., T. K. Rockwell, T. J. Middleton, and K. W. Hudnut (2012), Lidar and field observations of slip distribution for the most recent surface ruptures along the central San Jacinto Fault, *Bull. Seismol. Soc. Am.*, *102*(2), 598–619, doi:10.1785/0120110068.

Scharer, K. M., J. B. Salisbury, J. R. Arrowsmith, and T. K. Rockwell (2014), Southern San Andreas Fault evaluation field activity: Approaches to measuring small geomorphic offsets—Challenges and recommendations for active fault studies, *Seismol. Res. Lett.*, *85*(1), 68–76.

Schlagenhauf, A., I. Manighetti, L. Benedetti, Y. Gaudemer, R. Finkel, J. Malavieille, and K. Pou (2011), Earthquake supercycles in central Italy, inferred from $^{36}$Cl exposure dating, *Earth Planet. Sci. Lett.*, *307*, 487–500, doi:10.1016/j.epsl.2011.05.022.

Scholz, C. (2010), Large earthquake triggering, clustering, and the synchronization of faults, *Bull. Seismol. Soc. Am.*, *100*(3), 901–909, doi:10.1785/0120090309.

Scholz, C. H., C. A. Aviles, and S. G. Wesnousky (1986), Scaling differences between large interplate and intraplate earthquakes, *Bull. Seismol. Soc. Am.*, *76*(1), 65–70.

Sherrod, B. L., T. M. Brocher, C. S. Weaver, R. C. Bucknam, R. J. Blakely, H. M. Kelsey, A. R. Nelson, and R. A. Haugerud (2004), Holocene fault scarps near Tacoma,Washington, USA, *Geology*, *32*, 9–12.

Sieh, K. E. (1978), Slip along the San Andreas Fault associated with the great 1857 earthquake, *Bull. Seismol. Soc. Am.*, *68*(5), 1421–1448.

Sieh, K. E. (1984), Lateral offset and revised dates of large prehistoric earthquakes at Pallett Creek, southern California, *J. Geophys. Res.*, *89*(B9), 7641–7670, doi:10.1029/JB089iB09p07641.

Stirling, M., M. Gerstenberger, N. Litchfield, G. McVerry, W. Smith, J. Pettinga, and P. Barnes (2008), Seismic hazard of the Canterbury region, New Zealand: New earthquake source model and methodology, *Bull. N. Z. Soc. Earthquake Eng.*, *41*(2), 51–67.

Stirling, M., G. McVerry, M. Gerstenberger, N. Litchfield, R. Van Dissen, and K. Berryman (2012), National seismic hazard model for New Zealand: 2010 update, *Bull. Seismol. Soc. Am.*, *102*(4), 1514–1542, doi:10.1785/0120110170.

Stirling, M. W., S. G. Wesnousky, and K. Shimazaki (1996), Fault trace complexity, cumulative slip, and the shape of the magnitude-frequency distribution for strike-slip faults: A global survey, *Geophys. J. Int.*, *124*(3), 833–868.

Tapponnier, P., F. J. Ryerson, J. Van der Woerd, A.-S. Mériaux, and C. Lasserre (2001), Long-term slip rates and characteristic slip: Keys to active fault behaviour and earthquake hazard, *Earth Planet. Sci. Lett.*, *333*, 483–494.

Tonkin, P. J., and P. C. Almond (1998), Using the soil stratigraphy of loess to reconstruct the late Quaternary history of piedmonts adjacent to large strike-slip faults, South Island, New Zealand, *Geol. Soc. N. Z. Misc. Publ.*, *101A*, 227.

Van der Woerd, J., F. J. Ryerson, P. Tapponnier, Y. Gaudemer, R. Finkel, A. S. Mériaux, M. Caffee, G. Zhao, and Q. He (1998), Holocene left slip-rate determined by cosmogenic surface dating on the Xidatan segment of the Kunlun Fault (Qinghai, China), *Geology*, *26*, 695–698.

Van der Woerd, J., P. Tapponnier, F. J. Ryerson, A.-S. Meriaux, B. Meyer, Y. Gaudemer, R. C. Finkel, M. W. Caffee, Z. Guoguang, and X. Zhiqin (2002), Uniform postglacial slip-rate along the central 600 km of the Kunlun Fault (Tibet), from $^{26}$Al, $^{10}$Be, and $^{14}$C dating of riser offsets, and climatic origin of the regional morphology, *Geophys. J. Int.*, *148*, 356–388.

Van der Woerd, J., Y. Klinger, K. Sieh, P. Tapponnier, F. J. Ryerson, and A.-S. Mériaux (2006), Long-term slip rate of the southern San Andreas Fault from $^{10}$Be-$^{26}$Al surface exposure dating of an offset alluvial fan, *J. Geophys. Res.*, *111*, B04407, doi:10.1029/2004JB003559.

Van Dissen, R. J. (1989), Late Quaternary faulting in the Kaikoura region, southeastern Marlborough, New Zealand, MSc thesis, Oregon State Univ., Corvallis, Orig.

Wallace, L. M., J. Beavan, R. McCaffrey, K. Berryman, and P. Denys (2007), Balancing the plate motion budget in the South Island, New Zealand using GPS, geological and seismological data, *Geophys. J. Int.*, *168*(1), 332–352.

Wallace, R. E. (1968), Notes on stream channels offset by the San Andreas Fault, southern Coast Ranges, California, in *Proc. of Conf. on Geologic Problems of the San Andreas Fault System*, *Stanford Univ. Publ. in the Geol. Sci.*, vol. 11, edited by W. R. Dickinson and A. Grantz, pp. 6–21, Stanford Univ., Stanford, Calif.

Wallace, R. E. (1990), *The San Andreas Fault System, California*, pp. 14–58, US Government Printing Office, Washington, D. C.

Walsh, J. J., W. R. Bailey, C. Childs, A. Nicol, and C. G. Bonson (2003), Formation of segmented normal faults: A 3-D perspective, *J. Struct. Geol.*, *25*(8), 1251–1262, doi:10.1016/S0191-8141(02)00161-X.

Wells, D. L., and K. J. Coppersmith (1994), New empirical relationships among magnitude, rupture length, rupture width, rupture area, and surface displacement, *Bull. Seismol. Soc. Am.*, *84*(4), 974–1002.

Wesnousky, S. G. (2006), Predicting the endpoints of earthquake ruptures, *Nature*, *444*(7117), 358–360.

Wesnousky, S. G. (2008), Displacement and geometrical characteristics of earthquake surface ruptures: Issues and implications for seismic-hazard analysis and the process of earthquake rupture, *Bull. Seismol. Soc. Am.*, *98*(4), 1609–1632, doi:10.1785/0120070111.

Wood, R. A., J. R. Pettinga, S. Bannister, G. Lamarche, and T. J. McMorrran (1994), Structure of the Hanmer strike-slip basin, Hope Fault, New Zealand, *Geol. Soc. Am. Bull.*, *106*(11), 1459–1473.

Yang, J. S. (1991), The Kakapo Fault—A major active dextral fault in the central North Canterbury-Buller regions of New Zealand, *N. Z. J. Geol. Geophys.*, *34*(2), 137–143.

Yeats, R. S., and C. S. Prentice (1996), Introduction to special section: Paleoseismology, *J. Geophys. Res.*, *101*(B3), 5847–5853, doi:10.1029/95JB03134.

Yeats, R. S., K. Sieh, and C. R. Allen (1997), *The Geology of Earthquakes*, pp. 568, Oxford Univ. Press, New York.

Zielke, O., and J. R. Arrowsmith (2012), LaDiCaoz and lidar imager—MATLAB GUIs for lidar data handling and lateral displacement measurement, *Geosphere*, *8*(1), 206–221.

Zielke, O., J. R. Arrowsmith, L. G. Ludwig, and S. O. Akçiz (2010), Slip in the 1857 and earlier large earthquakes along the Carrizo Plain, San Andreas Fault, *Science*, *327*(5969), 1119–1122.

Zielke, O., J. R. Arrowsmith, L. G. Ludwig, and S. O. Akciz (2012), High-resolution topography-derived offsets along the 1857 Fort Tejon earthquake rupture trace, San Andreas Fault, *Bull. Seismol. Soc. Am.*, 1135–1154, doi:10.1785/0120110230.